To the Graduate Council:

I am submitting herewith a dissertation written by John Paul Gibbons, Jr. entitled "Production and Transport of Convoy Electrons." I have examined the final copy of this dissertation for form and content and recommend that it be accepted in partial fulfillment of the requirements for the degree of Doctor of Philosophy, with a major in physics.

Stuart B. Elston

Stuart B. Elston, Major Professor

We have read this dissertation
and recommend its acceptance:

John C Bloor

Leo S. Riedinger

Dan Fellers

Accepted for the Council:

Lewis Winkel

Associate Vice Chancellor
and Dean of The Graduate School

PRODUCTION AND TRANSPORT OF CONVOY ELECTRONS

A Dissertation

Presented for the

Doctor of Philosophy

Degree

The University of Tennessee, Knoxville

John P. Gibbons, Jr.

August 1991

ACKNOWLEDGEMENTS

I would like to acknowledge the leadership and advice given me as I have worked on this degree by both my major professors, Dr. Stuart B. Elston, and Dr. Ivan A. Sellin. Also, I would like to thank Dr. Robert DeSerio for his advice, especially relating to the numerical analysis of the data, and Dr. Joachim Burgdörfer for his advice pertaining to the theoretical aspects of this work. I would also like to thank Drs. Kenji Kimura, Jean-Pierre Grandin, Amine Cassimi, Michel Druetta, and Leif Liljeby for their participation in the data accumulation, and the staff members of GANIL facility for their assistance in performing the experiment upon which this dissertation is based.

Finally, I would like to thank my family, Becky, Valerie, and Britt, for their patience during the many long hours I spent on some aspect of this work.

ABSTRACT

Results are presented of doubly-differential (in energy and angle) cross section (DDCS) measurements for production of convoy electrons from 36 MeV/u Ar^{15+}, Ar^{17+}, and Ar^{18+} ions in thin amorphous carbon foils. The observed electron emissions are fitted to a multipole expansion of the DDCS, frequently employed to characterize ion-atom electron-loss to the continuum (ELC) and electron-capture to the continuum (ECC) cusp shapes. Thinner target data agree reasonably well with ion-atom predictions of component multipole moments, β_k. The results also reveal a rapid evolution of β_k with increasing target thickness. A quantitative model of the multipole evolution bridging the transition from the single- to the plural-collision regime is presented which demonstrates significant competition between one-step and multi-step production mechanisms. Excellent agreement is found for the first two even-ordered moments, β_2 and β_4, while the lack of good agreement for the dipole moment, β_1, suggests the need to include additional continuum electron transport phenomena.

Contents

List of Figures

List of Tables

Chapter 1

INTRODUCTION

> The phenomenon of the scattering and stopping of high speed atomic particles in passing through matter and the accompanying ionization and radiation effects have, as is well known, been one of the most important sources of information regarding the constitution of atoms. Ever since the pioneering work of THOMSON and RUTHERFORD, the analysis of the penetration phenomena has been in continual progress and has, in particular, offered many important tests of the gradually refined methods of atomic mechanics.[1] *Niels Bohr*, 1948.

As pointed out in the quotation by Bohr, the study of collisions between ionic projectiles and solid matter has been actively pursued since the birth of quantum mechanics. Furthermore, this interest has dramatically increased in recent years.[2] Nevertheless, despite such active interest in this field, there is still little understanding of the dynamics of many fundamental elastic and inelastic collisional phenomena.[3,4,5] This is mainly due to the fact that the description of ion-solid interactions is a very complicated problem—much more complicated than, for example, the related problem of describing ion-gas (or ion-atom) interactions. However, some recent theoretical progress[6] has been made in this area with, for example, the use of high-speed computer calculations.[7]

Of particular recent interest is the existence and/or population of projectile excited-states in fast ion-solid collisions. There is much debate over the existence of excited-states in a solid, particularly when the mean radius of the electron's orbit is larger than the interatomic spacing of the target.[8] Besides these obvious geometric limitations, the electrostatic screening by the target's conduction electrons also limit bound-state existence. Brandt and Richie[3,9] have attempted to describe this effect by writing the effective potential of the projectile Z_p in the solid as

$$V(r) = \frac{Z_p}{r} e^{-r/d}, \tag{1.1}$$

where the screening length, d, is given by the projectile velocity v_p, divided by the target's plasma frequency ω_p. While the number of bound states for a Coulomb potential is infinite, the screened Coulomb potential of Eq. 1.1 only supports a finite number of bound-states.[10]

In addition to these limitations, the effects of "collisional broadening" of the projectile's excited states create limitations on the number of *discrete* bound states. Electrons in projectile excited states undergo frequent inelastic collisions with target electrons which, from uncertaintly principle considerations, broadens the range of final state energies to be populated. This collisional broadening in effect produces a continuum of final states above a critical value of n, for which the broadening exceeds the level spacing. These three constraints are shown quantitatively in Figure 1.1, where the various limitations on the number of discrete principal quantum numbers n for the case of hydrogenic Ar^{17+} ions penetrating amorphous carbon are plotted as a function of velocity.[7]

Many experimental studies of projectile excitation in ion-solid collisions have been performed in recent years. Betz *et al.*[11] measured the Kα and Kβ x rays emitted from hydrogenic and heliumlike sulfur ions exiting carbon targets of varying thickness. These x rays were measured at centimeter distances behind the foil, where only high-lying Rydberg states have lifetimes long enough to contribute substantially to the spectra. Since these states were not expected to exist in the solid,

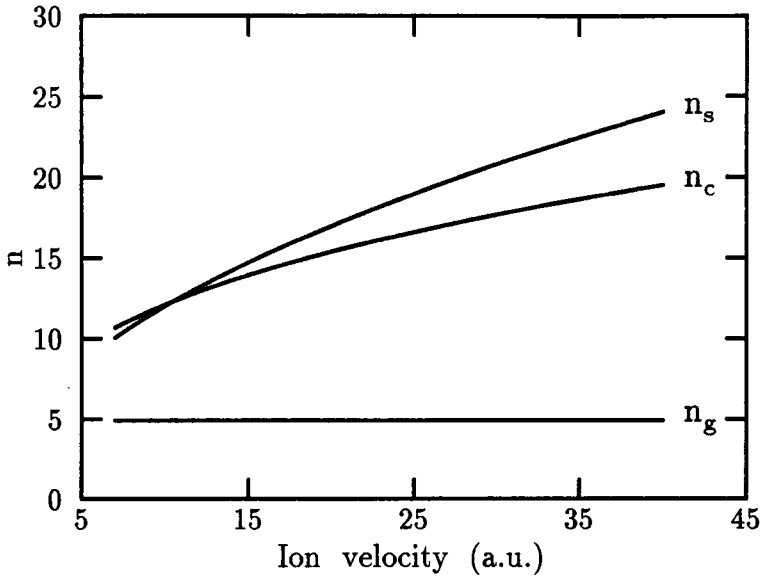

Figure 1.1: Maximum allowed principal quantum numbers for Ar^{17+} ions penetrating amorphous carbon. n_g: geometric limit; n_s: screening limit; n_c: collisional broadening limit.

it was assumed that they were produced in the last layer of the target. However, the measured x ray intensity normalized to the incident beam current indicated that the number of excited-states observed was much too high to be explained by the "last-layer" production hypothesis. Furthermore, analysis of their target thickness-dependent data[12] suggested the population of unusually high angular momentum states. Betz *et al.* argued that since such states could not possibly exist inside the bulk their production must have occurred outside the target where the static and dynamic screening disappears and electrons could be captured into high nl states.

Yamazaki and coworkers[13] discovered high angular momenta electrons emitted in the Coster-Kronig transition $1s^2 2p5l \rightarrow 1s^2 2s\epsilon l'$ of C^{2+} projectiles excited by carbon targets. In harmony with Betz's results, these authors argued that the high-l Rydberg states, whose orbital radii exceed even the screened limit defined by Eq. 1.1, must have been populated after emergence from the foil.

Chevallier *et al.*[4] observed a velocity threshold for the existence of $He^+(3p)$ state

in amorphous carbon, in accord with the predictions of Eq. 1.1. The agreement between the threshold velocity and the theoretical predictions[10] for observation of bound states for the screened Coulomb potential was reasonable.

In addition to these investigations, experiments concerning "convoy electrons" have also been used as a probe of projectile excitation. When a projectile of velocity $\vec{v}_p$ traverses a thin solid target, a cusp-shaped peak in the velocity spectrum of ejected electrons occurs at an electron velocity $\vec{v}_e = \vec{v}_p$. These so-called convoy electrons populate low-lying continuum states of the projectile and therefore provide an excellent probe of threshold and near-threshold collision phenomena. In binary ion-atom collisions a similar peak is observed for electron-loss-to-the-continuum (ELC) and electron-capture-to-the-continuum (ECC) processes where the "cusp" electron comes from either the projectile or target respectively. A number of investigations have been made to determine whether convoy electrons originate from these binary ion-atom processes or, alternatively, from a solid-state process in the bulk or at the surface of the target.[14,15]. For heavy-ion-solid collisions, measurements of both the "shape" (i.e. electron emission distribution) and the yield of convoy electrons have suggested that the ELC process within the bulk of the solid is responsible for convoy production. Nevertheless, a number of marked differences exist between the shapes of ELC cusp and convoy electron distributions, arguably due to the population of highly-excited projectile states inside the bulk of the solid. Thus, as an extension to this argument, the shape of the convoy electron distribution provides information about the level of projectile excitation within the solid.

To explore the evolution of convoy electron angular distributions from their binary atomic collision origins, an investigation of the transition from single to plural collision conditions for convoy electron formation has been performed. This work concerns this investigation and the interpretation of the results in terms of binary atomic collision cross sections. The emphasis of this measurement is placed on the shape of the convoy electron distributions, although the yields will be discussed in

terms of the modeling of the results. First, a discussion of earlier work concerning both ELC and convoy electron measurements is given. Secondly, the experimental apparatus used to accumulate the data will be described. Thirdly, the method by which the data are reduced and analyzed will be detailed. Finally, the results will be modeled in terms of atomic collision parameters.

1.1 Historical Background

1.1.1 Role of ELC in Convoy Electron Production

Although many different theories for ECC[16,17,18,19] and ELC[20,21] were published in the early to mid 1970's, they all predicted an isotropic electron emission distribution in the projectile rest-frame. However, measurements[22,23] of the energy distributions of ECC electrons revealed an asymmetric shape, skewed towards lower lab-frame energies. This asymmetry did not appear in either ELC or convoy electron energy distributions[24]. A sample of ELC and ECC longitudinal velocity distributions is shown in figure 1.2.

In addition to the shape similarities of ELC and convoy energy distributions, yield measurements provided further support for the role of ELC in convoy electron production. Hülskötter *et al.*[25] examined the exit charge-state dependences of convoy electron yields for fast (0.5, 1 MeV/u) Cl, Si and O projectiles on carbon foils of equilibrium thickness. Equilibrium thickness was defined as the thickness necessary to erase the memory of the initial charge state q_i of the incident projectile.[25] It was found that for these fast heavy-ion-solid collisions, the exit-charge state dependence of the convoy electron yields, coincident with exit-charge q_e, surprisingly showed no general trend when normalized to the number of exiting ions of charge q_e. This normalization would be appropriate if ECC was the dominant formation mechanism. However, when the data were renormalized to the number of exiting ions of charge $q_e - 1$, the appropriate normalization if ELC was the most impor-

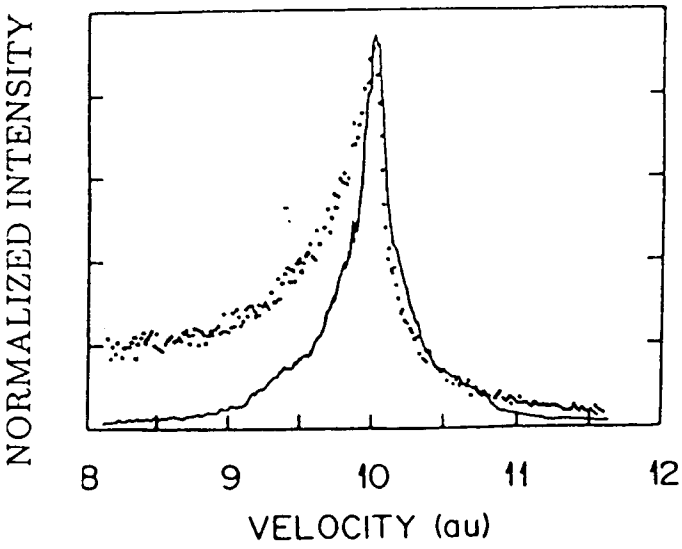

Figure 1.2: Comparison of ELC and ECC distributions. The points represent an ECC measurement; the solid line represents an ELC measurement.

tant process, the data followed a q_e^{-4} dependence, in agreement with the predicted charge-state dependence of electron loss[26].

A subsequent experiment by Yamazaki *et al.*[27], investigating the sub-equilibrium thickness-dependence of convoy yields for 2 MeV/u C ions incident on carbon foils, demonstrated that ELC dominated the observed experimental data, even when bare carbon ions were incident. This latter process was explained qualitatively by a two-step process involving the capture of a target electron into a projectile bound-state followed by an ELC event of that electron in the last few layers of the target. In both this experiment and Hülskötter's, all observed convoy energy distributions appeared symmetric about the cusp velocity as in the case for ELC.

1.1.2 Multipole Characterization of the Cross Section

In order to quantitatively parameterize the observed ECC asymmetry, a multipole expansion of the laboratory-frame differential cross section was introduced[28],

$$\frac{d\sigma}{d\vec{v}_e} = \frac{1}{v_e}\sum_{j,k}\beta_{j,k}v_e^j P_k(\cos\vartheta_e), \tag{1.2}$$

where v_e and ϑ_e represent the projectile-frame electron velocity and polar emission angle respectively. The v_e singularity produces the observed cusp-shaped peak; the $\beta_{j,k}$-parameters (other than $\beta_{j,0}$) produce any anisotropies seen in the data. Historically, this form of the cross section was an extension of previous results describing both ECC and ELC. For ECC processes, Lucas *et al.*[29] had found improvement in the description of their ECC data by adding a p-wave contribution resulting in a differential cross section of the form $v_e^{-1}(1 + D\cos\vartheta_e)$. For ELC processes, Briggs and Day[30] had predicted (within the first-Born approximation) a differential cross section of the form

$$\frac{d\sigma}{d\vec{v}_e} = \frac{1}{v_e}(1 + \beta_2 P_2(\cos\vartheta_e)), \tag{1.3}$$

for ELC from $1s$ states of hydrogenic-projectiles.

It is important to point out that the "forward-backward" asymmetry observed for ECC cusps in singly-differential energy measurements results from anisotropic emission about the *transverse* velocity axis (i.e. $\vartheta_e = \pi/2$) in the projectile-frame. Since even-order Legendre polynomials of argument $\cos\vartheta_e$ are symmetric about $\vartheta_e = \pi/2$, their presence in the differential cross section would produce no observable asymmetries in these type of measurements. ECC cusps therefore require non-zero contributions of odd-order Legendre polynomials.

In extending the earlier calculations of ELC processes by Briggs and Day, Burgdörfer[31] has utilized a group-theoretical approach to calculate the emission distributions for electrons emitted from arbitrary states nlm. In his first-Born calculation, the assumption is that the projectile velocity is much greater than the initial orbital

velocity of the projectile bound-state electron $v_{\rm orb}$, or

$$\frac{v_{\rm orb}}{v_p} \ll 1. \tag{1.4}$$

Within this assumption, Burgdörfer finds that for ELC from an initial projectile bound-state of principal quantum number n, no odd- and only even-order multipoles $\beta_{0,k}$, with $k \leq 2n$, will be present in the data. Thus, a measurement sensitive to the presence of even-order moments $\beta_{0,k}$ may indicate the population of projectile bound-states $n = k/2$ within the solid.

This prediction agreed well with the data of Elston *et al.*[32] and Berry[33] who measured doubly-differential (in energy and angle) electron emission distributions for the collision systems O^{5+} + He and O^{5+} + Ar at collision energies of 41, 82 and 105 MeV. For this particular collision system, cusp electrons were produced primarily by ELC of the more loosely bound $n = 2$ electron and, as predicted by Burgdörfer, emission distributions were adequately described by inclusion of only even-order multipole moments $\beta_{0,0}, \beta_{0,2}$ and $\beta_{0,4}$.

Berry *et al.*[8] extended the doubly-differential measurements described above to include collisions with thin self-supporting amorphous carbon targets. The resulting convoy electron emission distributions, like the previous ELC cusp distributions, contained no significant odd-multipole content. However, these distributions were noticeably more transverse than the corresponding ELC distributions. This can be seen in Figure 1.3, where 20% contours of ELC (with Ar targets) and convoy electron emission distributions have been plotted for all three collision velocities. Furthermore, it was found that the convoy electron data contained high even-order multipoles, up to $\beta_{0,10}$. Berry *et al.* concluded that these high order moments indicated the presence of highly excited projectile bound states within the bulk of the solid.

In an effort to investigate this conclusion, we extended Berry's measurements to include foil targets of varying thicknesses. These measurements were made using 115 MeV $O^{5,7,8+}$ ions (v_p = 17 a.u.) produced by the Holifield Heavy Ion Research

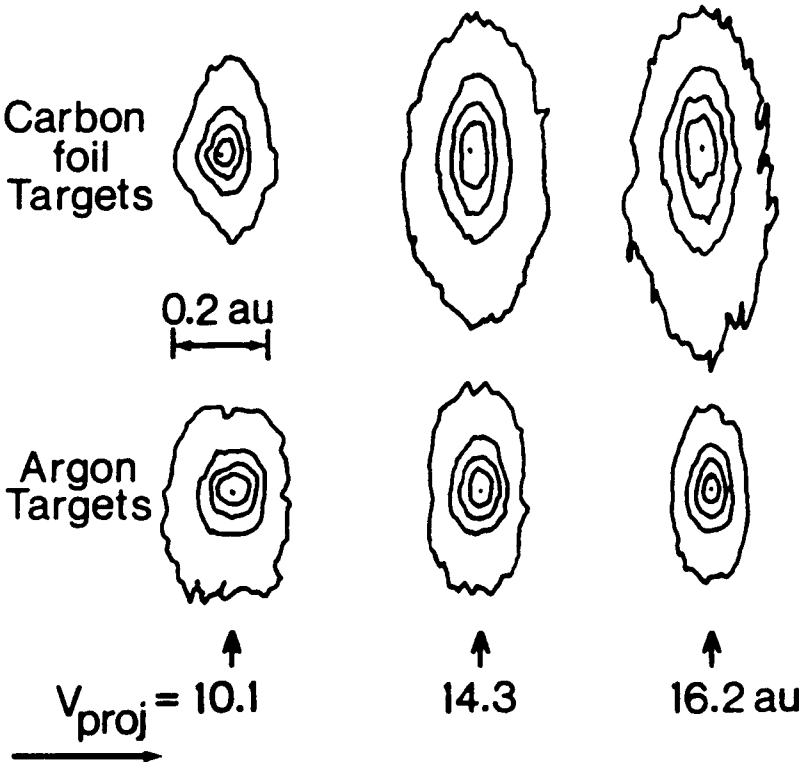

Figure 1.3: Comparison of ELC and convoy electron emission distributions. Isotropic emission would give rise to approximately circular contours. From Reference 8.

Facility (HHIRF). By measuring the thickness-evolution of multipole content (particularly high even-order $\beta_{0,k}$), we sought to probe the evolution of the state of excitation of the projectile as a function of dwell time in the solid. However, utilizing targets ranging upwards from the thinnest available carbon foils ($\sim 1\mu g/cm^2$, or $\sim 50\mathring{A}$)—far thinner than the thickness required for charge state equilibration for the incident oxygen beam—we found no significant evolution of multipole content. Furthermore, as in Berry's results, these data contained high-order multipoles to order $k \sim 10$. These results were interpreted as being due to an extremely rapid population of excited states, within the first few layers of the target.

Thus, in order to test this hypothesis, and to view the evolution of convoy electron distributions from their ion-atom counterparts, it was necessary to make further measurements using faster incident projectile ions. In order to satisfy this requirement, application was made for experimental beam time at the GANIL cyclotron facility in Caen, France, where projectile energies meeting this criterion were easily obtainable. These measurements which form the basis of this work took place in May 1990.

Chapter 2

EXPERIMENT

In order to study the rapid evolution of convoy electron distributions, it was necessary to acquire beam-time on an accelerator capable of providing extremely fast, highly-charged ionic projectiles. Furthermore, it was also necessary for this beam of particles to be well collimated in both radial size and angular divergence. These requirements were met by the GANIL (Grand Accélérateur National d'Ions Lourds) cyclotron facility in Caen, France, which awarded seven eight-hour shifts of 36 MeV/u Ar^{15+} beams for this project. This particular collision system was chosen for several reasons. First, the corresponding convoy electron energy ($\sim$ 20 keV) is both much higher than the energy of the previous HHIRF measurement (by a factor 5) and still within the analyzing (or voltage) limits of the electrostatic spherical sector spectrometer available for use. Furthermore, this increase in convoy electron energy was deemed sufficient to increase the free electron mean-free-path to distances greater than the thickness of our thinnest targets. This requirement was made to reduce the scattering of the convoy electrons produced within the bulk—scattering which could, perhaps, influence the observed emission distributions. The velocity of this ion beam (v_p = 37 a.u.) also parallels previous ion-solid measurements of electron capture by bare 36 MeV/u Kr.[34] Finally, the ratio of the mean projectile bound-state velocity ($v_{orb} \approx Z_p/n$) to the corresponding ion velocity is of the order of $1/2n$. This ratio, critical in the application of first-Born approxi-

mations to electron loss (see Eq. 1.4), is approximately the same as that for the HHIRF data.

2.1 Accelerator and Beamline

The GANIL facility, constructed primarily to provide high-quality heavy ion beams with good energy resolution ($\Delta E/E \sim 10^{-3}$), consists of an electron cyclotron resonance (ECR) ion-source followed by a sequence of three cyclotron-accelerators[35]. A general lay-out of the facility is shown in Figure 2.1. An initial beam of Ar^{5+} was accelerated to 5.3 MeV/u in the first of two separated-sector cyclotrons (SSC1 and SSC2), striped to Ar^{15+} , and accelerated to 36 MeV/u in SSC2. The high energy beam was then energy analyzed and delivered into the experimental area where one of many beam lines (Gauche or Droit) of the main experimental line may be selected.

Since an ion beam from a cyclotron is pulsed rather than continuous, it was necessary to make sure that there would be no significant electronics dead-time errors due to one or more events occurring within the same beam pulse. For this experiment, the $\sim$ 10 MHz SSC resonator frequency provided a maximum of about 5×10^3 ions in a 10 nsec wide pulse, delivered every $\sim$ 100 nanoseconds. Since the convoy electron event rate was always at or below the maximum detection rate for our apparatus, $\sim$ 10 kHz, the cyclotron beam produced at most an average of 1 convoy electron event per 1000 pulses. Thus, the probability of having two events within a single pulse was negligible.

The experiment was located in target rooms D3 and D4 on the LISE facility (Ligne d'Ions Super Epluchés: beam line of highly stripped ions), which allowed further stripping of the Ar^{15+} beam to higher charge states Ar^{17+} and Ar^{18+} prior to the experiment. A schematic of these rooms is shown in Figure 2.2. The incoming beam is initially focused with magnetic quadrupoles $q1$—$q4$ onto a stripper foil (or

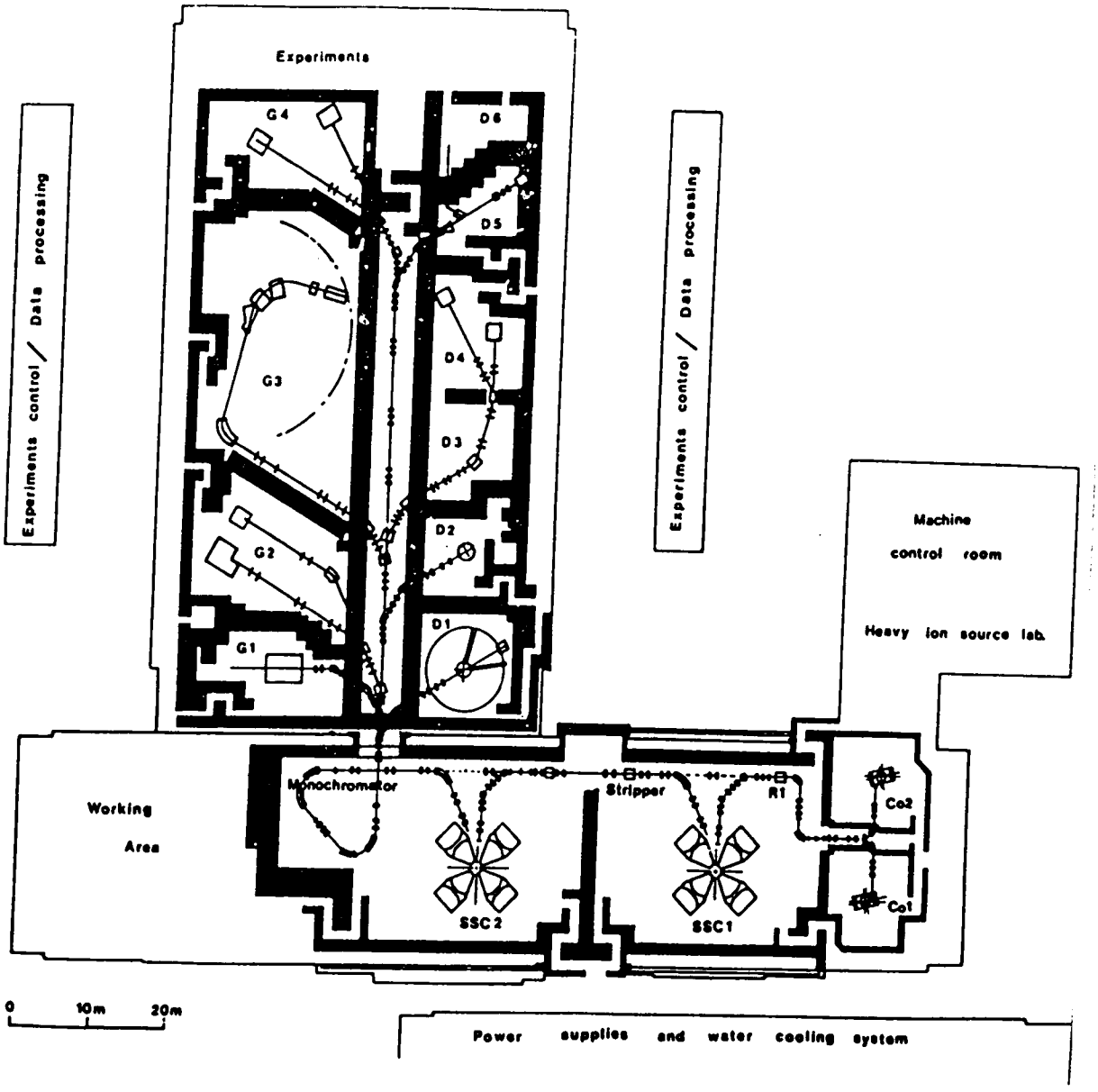

Figure 2.1: General lay-out of the GANIL facility.

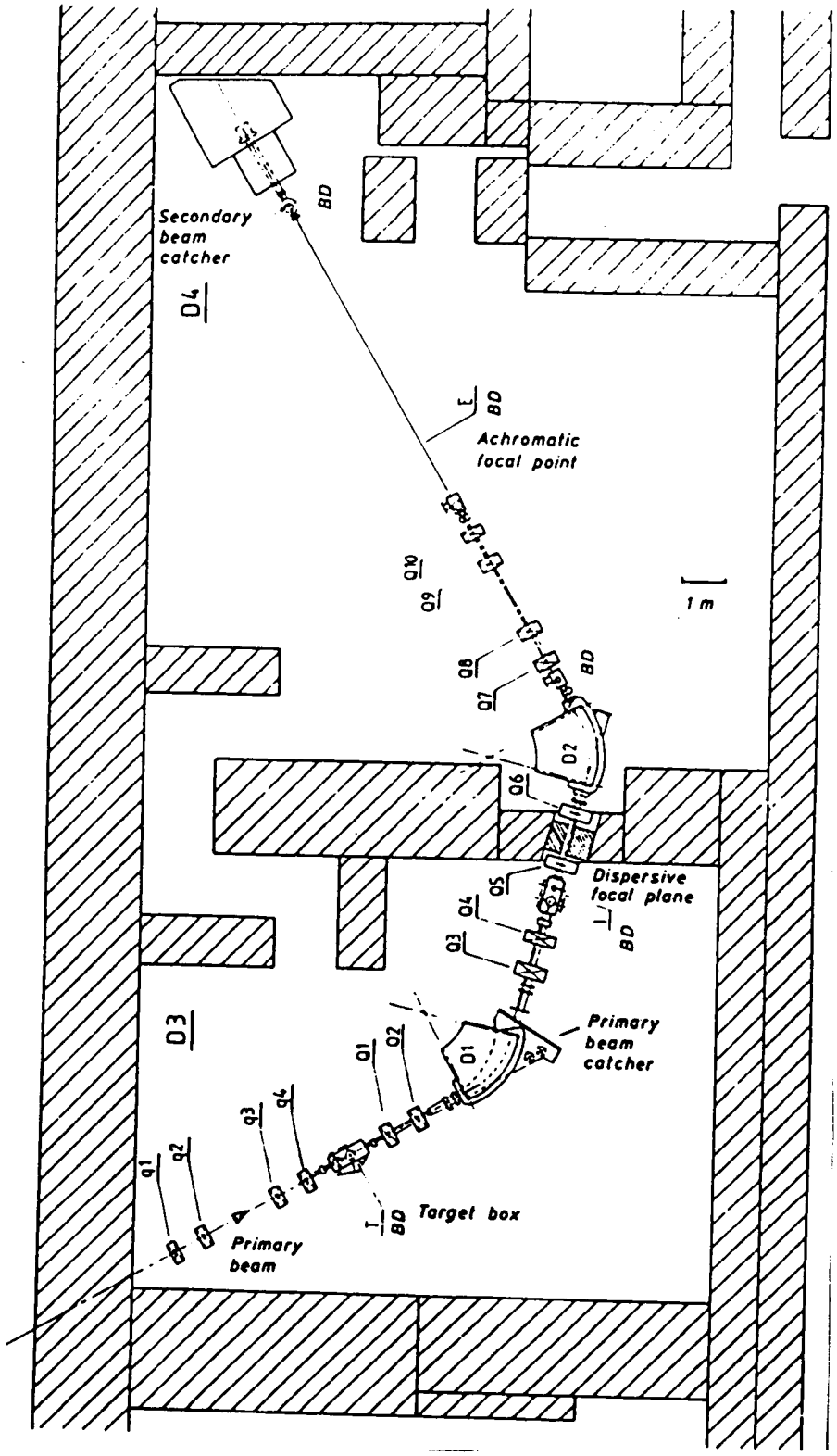

Figure 2.2: Experimental beam line LISE. BD indicates the main locations of the beam diagnostics.

an aperture when Ar^{15+} is desired) in room D3. The remaining steering elements are designed to achromatically focus[36] the stripped beam at the focal point shown in room D4. The scattering chamber was mounted on the beam line in D4 such that the carbon foil targets were positioned at this focal point, where the ion beam was focused electromagnetically to a 1.0 mm diameter with 0.36° angular divergence. The design of this facility was sufficient to require no physical collimation within the experimental area. This facet of LISE was very desirable for this measurement: collimating apertures or 4-jaw slits produce a spurious backgound of electrons which may be detected by the experimental apparatus.[33]

After traversing the experimental chamber in D4, the beam was collected on a Faraday cup located $\sim$ 6 meters downstream from the focal point. Unfortunately, the Faraday cup was not able to accurately measure currents <1 nA, primarily due to leakage currents within the cup as well as within the electrical connections to the current integrator located outside the target area. This presented a problem for Ar^{15+} incident on the thicker targets, where the convoy electron yields per incident ion were the largest ($\sim 10^{-4}$). For these cases, beam currents $\gtrsim$ 1 nA would produce an event rate greater than the maximum detection rate of the PSD and electronics ($\sim$ 10 kHz).

The vacuum throughout the beamline was kept below 10^{-6} Torr and was maintained by a system of (primarily) turbomolecular pumps. This pressure was sufficiently low enough to guarantee insignificant charge changing due to collisions with background gas.

Before beginning the convoy electron measurement, the exiting charge state fractions of Ar^{15+} incident on the stripping foils in D3 were measured using beam diagnostic equipment native to the LISE facility. In the target chamber in room D3 (BD T) a 10-position target wheel containing 4 carbon foils of thicknesses $\sim$ 100, 150, 200 and 500 $\mu g/cm^2$ was placed for stripping the Ar^{15+} beam. In addition to these thicker targets, five more positions on the wheel were filled by carbon foils

Table 2.1: Table of measured exiting charge state fractions for Ar^{15+} incident on carbon foils of varying thicknesses. The results are expressed as a percentage of the total number of exiting ions.

Thickness ($\mu g/cm^2$)	Ar^{15+} (%)	Ar^{16+} (%)	Ar^{17+} (%)	Ar^{18+} (%)
1.0	93.9	5.90	0.13	< .01
3.1	89.2	10.4	0.33	< .01
4.9	86.9	12.6	0.47	0.02
10.1	84.8	13.0	2.10	0.07
112	11.3	52.9	30.1	5.80
150	2.50	39.7	44.3	13.6
210	0.90	24.4	56.8	17.9
472	< .01	2.70	25.9	71.4

of thicknesses near those used in the convoy electron measurement in D4 (1—15 $\mu g/cm^2$). For each thickness, only charge states 15, 16, 17, and 18 were detected with any significance. For the thicker foils, the relative intensities of the exiting ions of different charge states were determined through direct (time) integration of the charge-selected beam current collected in a Faraday cup placed after the first dipole magnet (BD I). For the thinner foils where the percentage of the higher charge states (16, 17 and 18) was much lower, the intensities were determined with an Ar-CO_2-filled proportional wire chamber. After each charge state was selected and measured, the initial charge state was measured again to check for large, long-term changes in the beam current. The results of these measurements are listed in Table 2.1.

2.2 Target Chamber

Shown in Figure 2.3 is a rough block diagram of the 24-inch diameter stainless-steel scattering chamber placed in D4. The incoming ion beam passes through a parallel plate analyzer (PPA) used to deflect electrons from an electron gun (EG) onto the target wheel (TW) for foil thickness calibration (see below). The ion beam collides with a mounted target, passes through a hole in a spherical sector electrostatic analyzer (SSA), and exits the chamber. A layer of 0.01 inch thick μ-metal shielding was wrapped around a octagonally-shaped support structure within the chamber; the shielding was penetrated by several small holes made for electrical feedthroughs, beam transmission and vacuum pumping. Measurements of magnetic field intesity inside the chamber with and without the shielding indicated an average reduction of a factor 10 in field strength. A 1000 l/s cryopump and a 450 l/s turbopump mounted on the bottom of the chamber kept base pressures within the chamber below 10^{-8} Torr.

2.2.1 Spherical Sector Analyzer and Position Sensitive Detector

Electrons emitted from the target within a small forward angle of $\sim 6°$ were analyzed by an 160° electrostatic spherical sector analyzer pictured in Figure 2.4. This analyzer has been previously been described in detail[33,37,38], so only a brief description is given here. The analyzer consisted of two concentric copper spherical sectors with mean radius 55 mm and deflection angle of 160°. Compared with the original 180° design of Purcell[39], which provides stigmatic focussing to second order in the deflection plane and to infinite order in the plane perpendicular to the deflection plane, the 160° analyzer retains the focussing qualities to a good

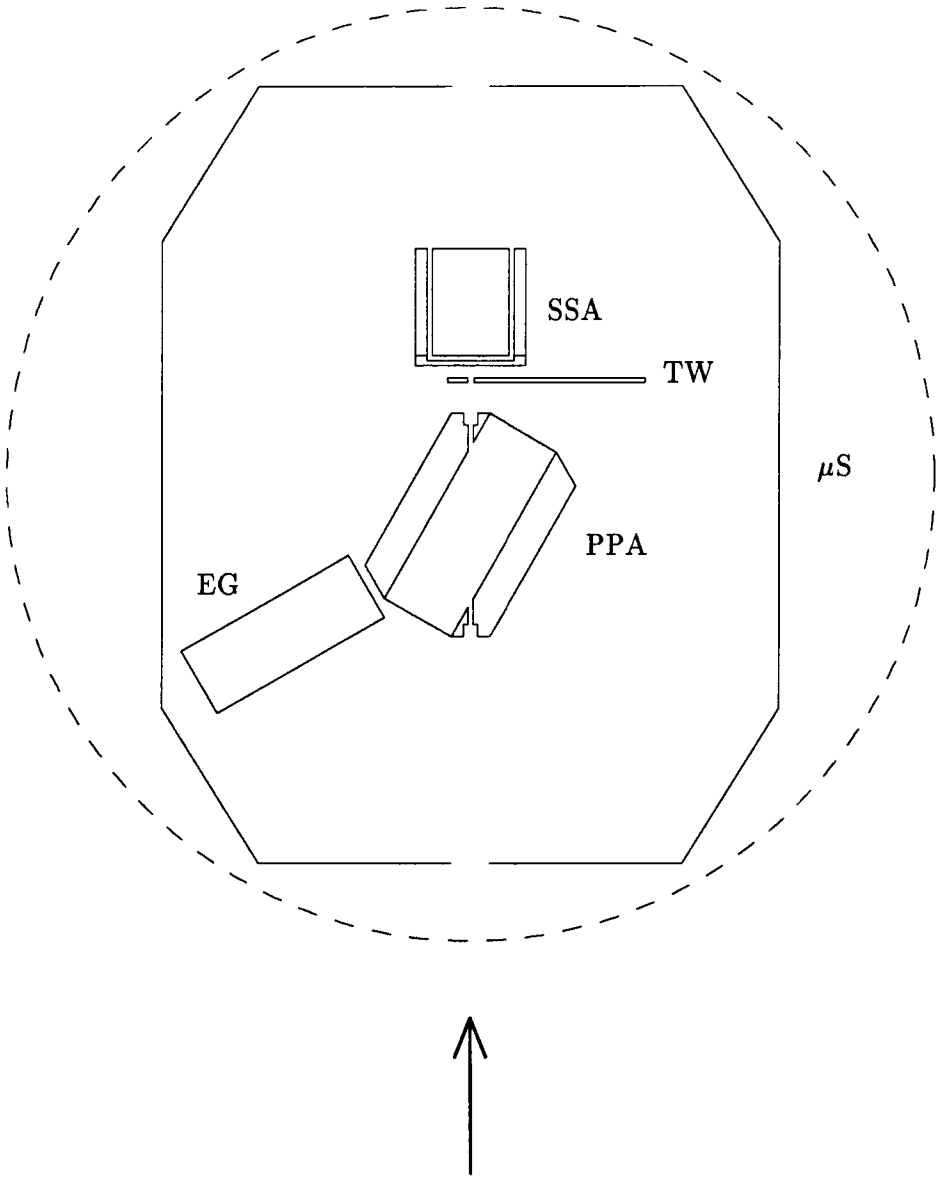

Figure 2.3: Block diagram of scattering chamber, scale 1:5. Arrow indicates ion beam direction. The position sensitive detector, placed at the exit of the spherical sector analyzer, is not shown. EG, PPA: Electron gun and parallel plate analyzer assembly; TW: Target wheel; SSA: Spherical sector analyzer; μS: Magnetic shielding.

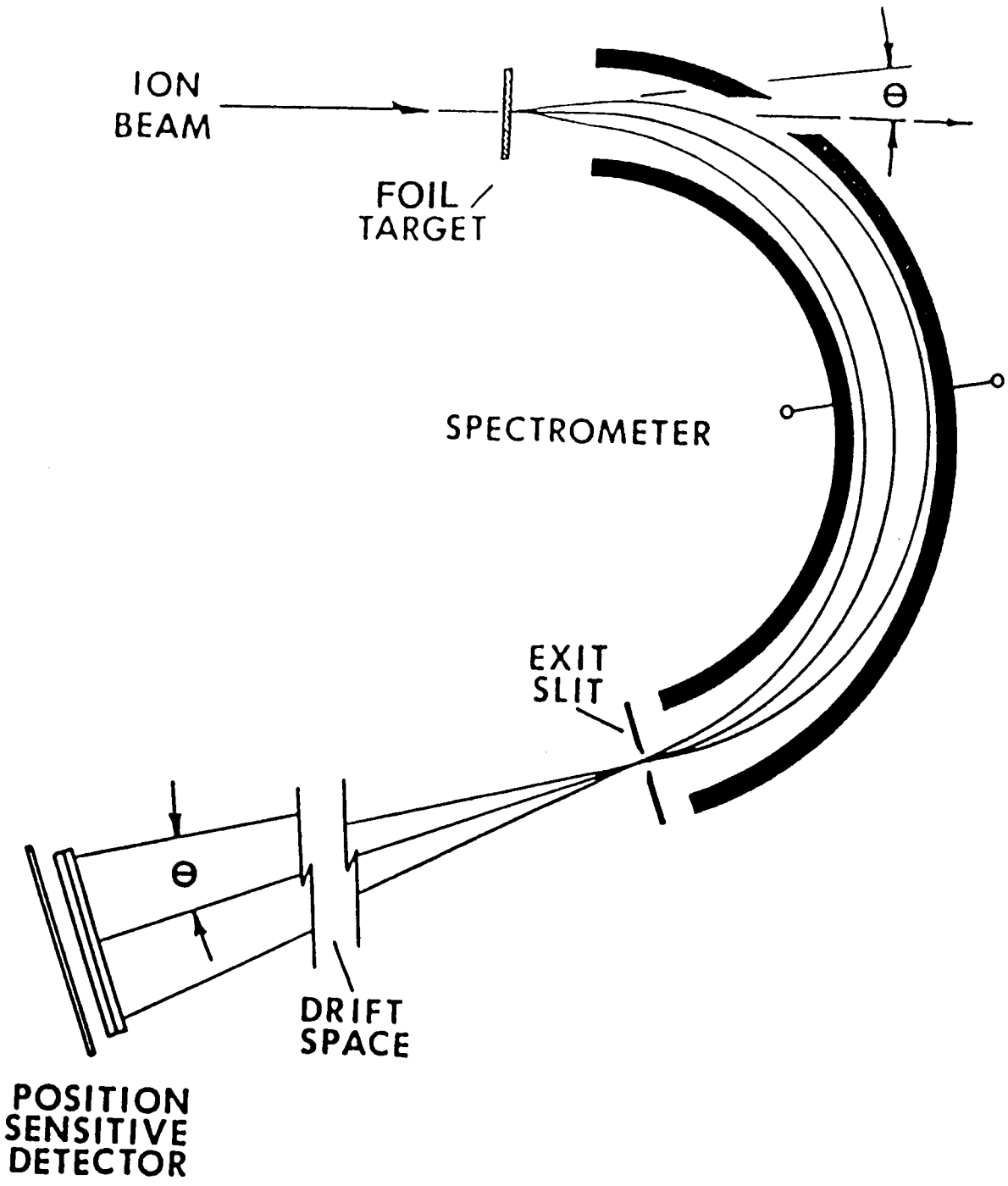

Figure 2.4: Electrostatic spherical sector analyzer.

degree[40] while removing the focal points from the field region. The energy-selected electrons arriving at the exit aperture reproduce their angular emission with respect to the central ray; that is, the trajectory of an energy-selected electron emitted at 0° in the lab-frame. The deflection voltages were applied to the outer (V_o) and inner (V_i) sectors by two programmable Glassman MJ-series power supplies (maximum voltage: +5kV, -6kV) in the fixed ratio V_o/V_i=-0.8041 so that the central trajectory was at ground potential. These two power supplies were programmed using a computer-controlled 16-bit DAC.

Electrostatic deflection spectrometers are characterized by an analyzer constant K which equals the ratio of the voltage difference $V \equiv V_i - V_o$ to the corresponding non-relativistic electron pass energy E_e. The analyzer constant of the device used in this experiment was K=0.449 volts/eV. Relativistically, the voltage required to deflect an electron with relativistic kinetic energy T_0 is given (in a.u.) by[42]

$$\frac{V}{K} = \frac{T_0}{2} + \frac{T_0}{2}(1 + \frac{T_0}{c^2}). \tag{2.1}$$

The energy selected electrons exiting the spectrometer traverse a 15 cm shielded drift region before being detected by a position sensitive detector (PSD) shown in Figure 2.5. The PSD consists of a tandem (chevronned) pair of microchannel plate electron multipliers followed by a circular-arc-terminated resistive anode. Four independent charge-sensitive pre-amplifiers connected to the corner of the resistive anode detect the relative proximity of the resulting event. A Surface Science Laboratories[43] Ratiometric Position Decoder then determines the relative horizontal (x) and vertical (y) positions on the anode which are output as two eight-bit digital quantities. For each electron incident on the front of the microchannel plate array, an avalanche of $\sim 10^6$ electrons exits the back with negligible change in relative position (from the central ray) and are accelerated to the resistive anode by an applied potential difference.

The PSD is mounted so that electrons following central-ray trajectories would be detected at the center of the anode. Thus, an electron having a lab-frame polar

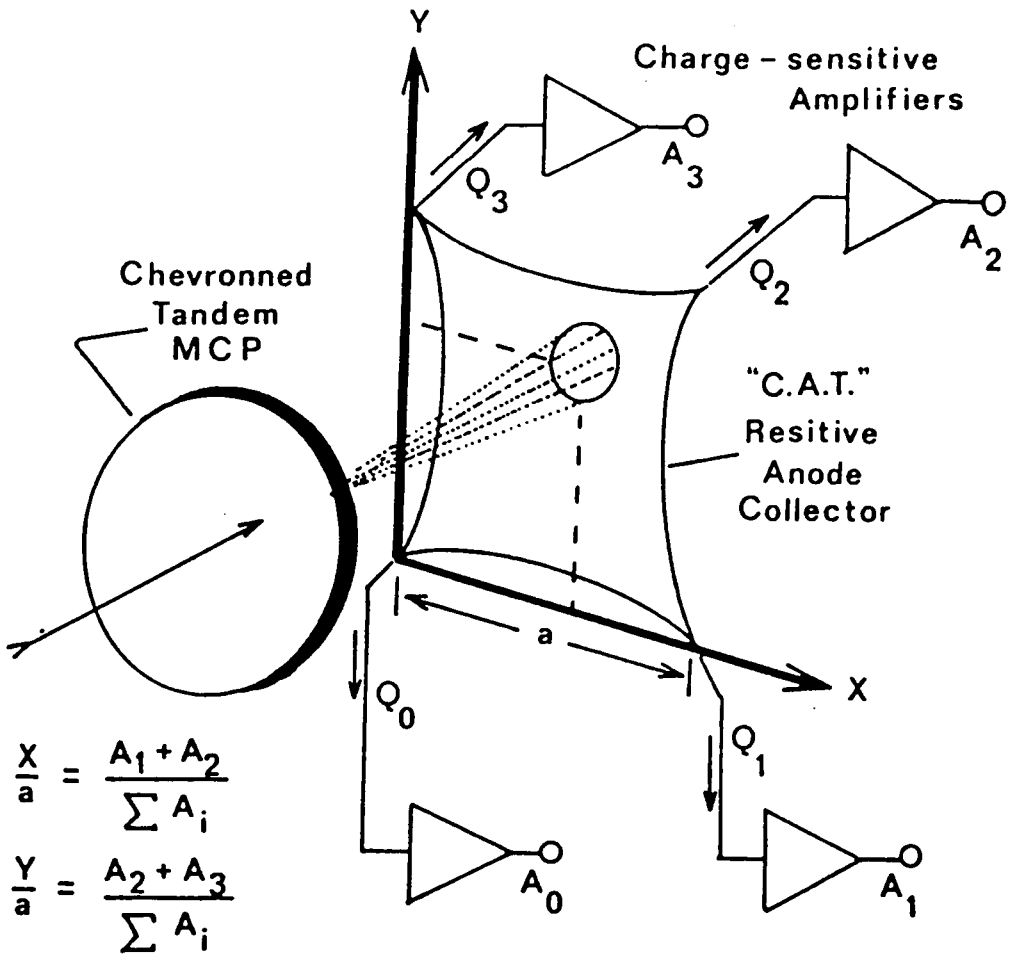

Figure 2.5: Schematic of the position sensitive detector. An incident electron creates an electron cascade within the multichannel plate (MCP) pair, which in turn produces a charge cloud collected on the resistive anode. The position of the event on the anode is found using the indicated ratios of the anode's four corner pickups.

emission angle θ_e is translated a distance $d = (15\ cm)\tan\theta_e$ from the center of the detector upon arrival at the detector surface. A 0.75 inch aperture placed in front of the PSD, at a distance of 5.3 inches from the spectrometer exit aperture, limited detection to electrons emitted with polar angles $\theta_e < 4°$.

2.2.2 Targets and Calibration

Carbon foil targets were purchased from the Arizona Carbon Foil Company over a range of $\sim$ 0.5—25 $\mu g/cm^2$ and with density $\rho = 2g/cm^3$. Foils with claimed thicknesses $\geq$ 1.0 $\mu g/cm^2$ were floated onto target holders with 4 mm diameter holes, while the thinnest 0.5 $\mu g/cm^2$ foils could only be floated onto target holders with 2 mm diameter holes. After the foils were dried and tested (see below), 13 different thicknesses were mounted on a 15-position target wheel (TW) and placed in the scattering chamber. The remaining two positions on the wheel contained an empty foil holder with a 4 mm diameter hole, used to check for background events not associated with the targets, and a red "phosphor" with a 2 mm hole, used for aligning the ion beam to the target wheel. The red phosphor was a chromium-doped alumina (Cr-Al_2O_3) wafer approximately 1 mm thick.

In order to calibrate foil thicknesses as well as simply to check the foils' survival after evacuation of the target chamber, a test source of electrons, consisting of an electron gun (EG) and a 30° parallel plate analyzer (PPA), was constructed. The analyzer was designed both to deflect the emitted electrons onto the target wheel at the corresponding focus of the SSA, as well as to allow passage of the ion beam during the experiment. The collimation of the electron gun was defined by a 1.0 mm aperture immediately following the source (a ribbon-type tungsten filament) and a 0.1 mm aperture 120 mm downstream, giving a maximum angular divergence of $\sim$ 4 mrad. Monoenergetic electrons emitted with different angles at the 0.1 mm aperture were refocussed (to second order) at the target. The PPA was further designed to allow an incident ion beam to pass unscathed and provide a

electrostatic "skimmer" of any background electrons travelling along with the beam. It was found that there was very little background associated with the ion beam so that this latter feature was unnecessary.

Before beginning the experiment, foil thicknesses were calibrated by measuring the energy loss distributions of v_p=11 a.u. electrons (1646 eV) incident on the range of foils on the target wheel. This energy was chosen to compare the results with those of Lencinas *et al.*[44] who measured the energy loss of 1646 eV electrons transmitted within a forward cone of half-angle 0.5° . After the filament of the electron gun had equilibrated ($\sim$ 1 hour), the energy distributions of electrons traversing a foil were found by scanning the voltage on the SSA versus time and detecting the energy-selected electrons transmitted within the 4° half-angle of the PSD. A typical dataset involved $\sim$ 50 scans over the chosen energy range, spending one second at each voltage of each scan. A sample of the data is shown in Figure 2.6.

The method by which these datasets were analyzed is taken from Ashley.[45] The experimental energy distribution of transmitted electrons with energy losses ω for a target of thickness x is compared with a calculated multiple scattering distribution, $f(x,\omega)$. The multiple-scattering distribution is found from the corresponding thickness-independent single-scattering distribution, or differential inverse mean free path (DIMFP), for inelastic scattering of electrons of energy E[45,46],

$$\frac{d\Lambda^{-1}}{d\omega} \equiv \tau(\mathrm{E},\omega) = \frac{1}{\pi \mathrm{E}} \int \frac{dq}{q} \mathrm{Im}\left\{\frac{-1}{\epsilon(q,\omega)}\right\}, \tag{2.2}$$

where ω and q represent the energy loss and momentum transfer respectively. $\mathrm{Im}\{-1/\epsilon(q,\omega)\}$ is the imaginary part of the negative reciprocal of the dielectric response function ϵ of the solid, which can be approximated by a sum of Drude-type functions[45]:

$$\mathrm{Im}\left\{\frac{-1}{\epsilon(q,\omega)}\right\} = \sum_{i=1}^{4} \frac{A_i \gamma_i \omega}{[(\omega_{0i} + q^2/2)^2 - \omega^2]^2 + (\gamma_i \omega)^2}. \tag{2.3}$$

The coefficients A_i, γ_i, and ω_{0i} were fitted by Ashley to match the optical energy-loss

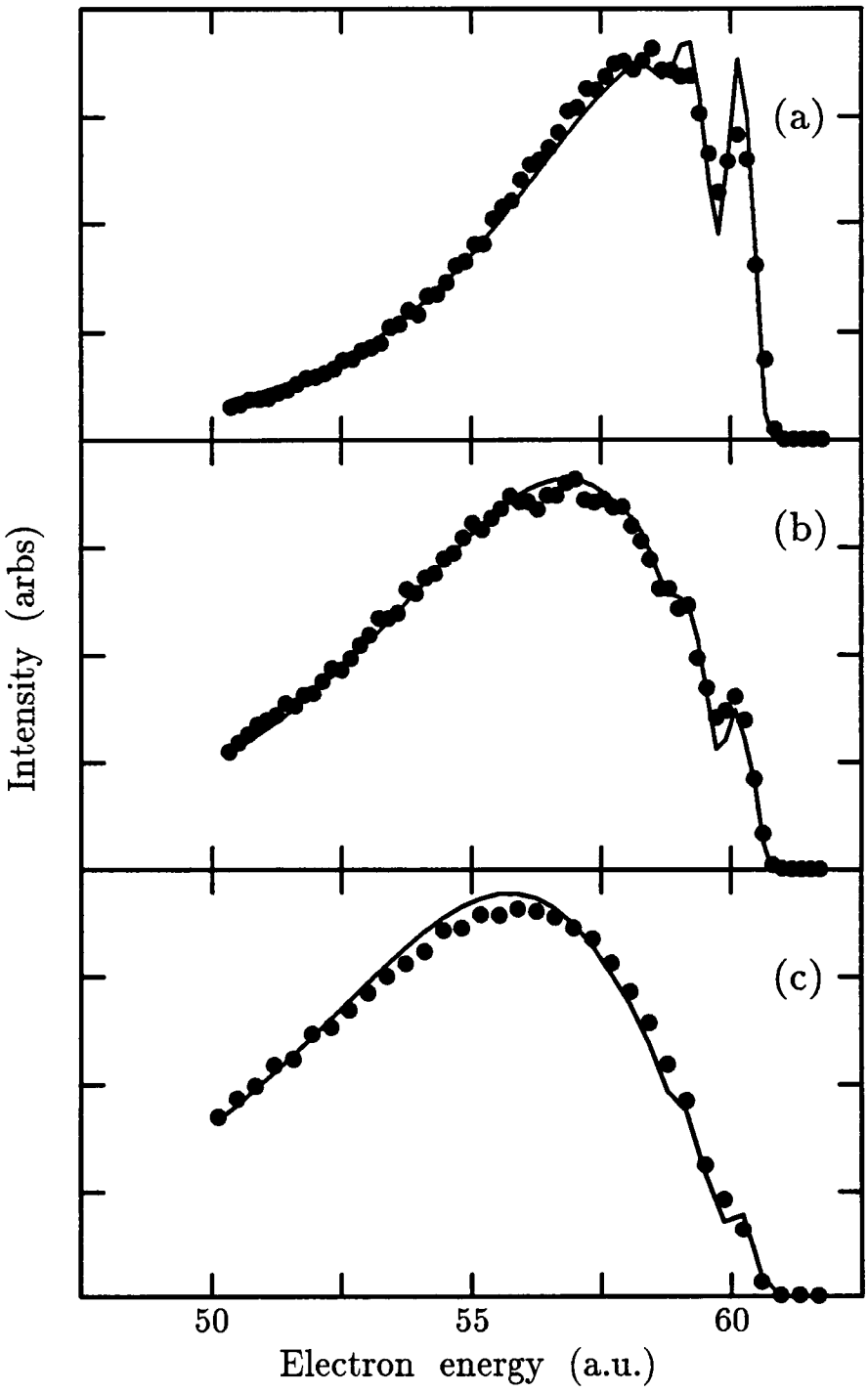

Figure 2.6: Free electron energy distributions after penetration through amorphous carbon foils. Electrons of energy 60.5 a.u. were incident on manufacturer's-claimed thicknesses (a) 0.5, (b) 1.5, (c) 2.6 $\mu g/cm^2$. The dots represent experimental data; the solid line represents a fit described in the text.

function, $\mathrm{Im}\{-1/\epsilon(0,\omega)\}$, with experimental data available for optical energy loss data on glassy carbon.[47] The resulting inelastic mean-free-path calculated from integration of Eq. 2.2 is 76 a.u. for 1646 eV electrons.

The DIMFP of Eq. 2.2 is proportional to the energy-loss distribution of an electron having a single collision. The calculated energy-loss distribution $f(x,\omega)$ after multiple collisions was obtained using a convolution technique developed by Williams.[48] This technique assumes that the range of energy loss ω is small compared to the initial energy E. In this case, the energy-loss distribution at thickness $2x$ is the convolution of the distribution at thickness x with itself:[45]

$$f(2x,\omega) = \int_0^\omega f(x,\omega-\omega')f(x,\omega')d\omega'. \tag{2.4}$$

Thus, if an initial distribution at thickness x_0 is known, the distribution at $2^N x_0$ can be found by doing N repetitions of Eq. 2.4.

If $x_0 \ll \Lambda$, then the initial distribution can be approximated as a sum of the zero- and single-scattering distributions:[45]

$$f(x_0,\omega) = (1-\frac{x_0}{\Lambda})\delta(\omega) + x_0\tau(\mathrm{E},\omega). \tag{2.5}$$

As evident in Eq. 2.2, the integral of $\tau(\mathrm{E},\omega)$ over all energy losses ω is Λ^{-1}. Thus the integral (over ω) of the distribution $f(x_0,\omega)$ is unity, as are all the integrals of all thicker-target distributions calculated from Eq. 2.4. The final distribution was found after 10 thickness-doublings as detailed in Eq. 2.4. In order to compare with the observed spectra, the final distribution $f(x,\omega)$ was multiplied by an overall amplitude to scale the normalized distribution to the intensity of the experiment. This amplitude represents the number of electrons transmitted within a forward cone of 4° during the total time spent in any channel. Recalling that the integral of $\tau(\mathrm{E},\omega)$ over energy loss is Λ^{-1}, Eq. 2.5 suggests a dimensionless measure of thickness x/Λ. Two parameters, the target thickness (in units of Λ) and the amplitude, were fitted to the experimental data using a non-linear least squares fitting routine[49]. A sample of resulting fits are shown as the solid lines in Figure 2.6.

As is evident in the figure, the agreement between the energy loss distributions of the data and fit is quite good. However, it was found that while the fits reproduced the shape of the electron energy loss distribution, the fitted thicknesses were approximately 1.5–2 times greater than the manufacturer's claimed values—far above the absolute error in thickness claimed by Arizona Carbon Foil Company ($\pm$ 1.0 $\mu g/cm^2$). Given that the multiple scattering distribution $f(x, \omega)$ utilized here does an excellent job reproducing the shape of the observed distributions, it is doubtful that this is the source of the problem. Two other possible sources of error may be responsible for this discrepancy: The targets could be 1.5–2 times thicker than Arizona claims, or the calculated mean-free-path may be 1.5–2 times too large.

In order to test the first hypothesis, optical transmission measurements were made on the carbon foils. The attenuation of a 40 mW He-Ne laser (λ= 6328 $\AA$) was measured after transmission through carbon foils of varying thicknesses evaporated onto glass slides. The foils used in the convoy electron measurement were taken from slides among those measured. The measured transmittance was compared with a transmittance formula based on Fresnel's equations for an absorbing film (carbon) on a nonabsorbing substrate (glass).[50] The complex index of refraction for evaporated carbon was found from previous measurements on foils from Arizona Carbon Foil Company.[51]. The results indicated that the carbon foil thicknesses agree, within the error of the measurement ($\sim$ 20%[52]), with the manufacturer's claimed results. Furthermore, while some thickening during the convoy electron measurement is possible[53], this process is expected to add only a constant amount of thickness to each foil.

Alternatively, the use of the calculated mean-free-path above (Λ = 76 a.u.) for glassy carbon may be in error. Substantial improvement in the thickness agreement was obtained renormalizing the DIMFP to the inelastic mean free paths calculated either from empirical data (Λ=42 a.u.)[54] or a free-electron gas model of the dielectric function $\epsilon(\Lambda$=43 a.u.).[55] A plot of the claimed thicknesses (with absolute

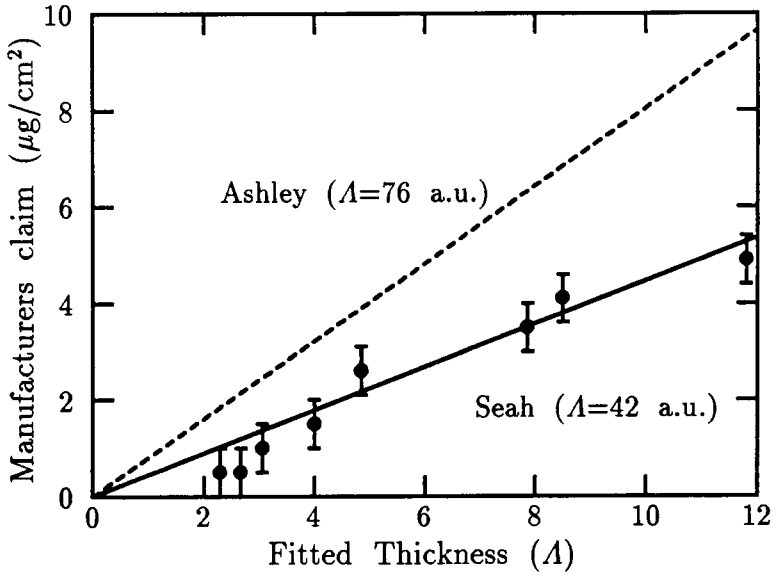

Figure 2.7: Plot of manufacturer-claimed thicknesses versus fitted results. Displayed error bars indicate absolute errors as claimed by the manufacturer. The statistical errors of the fit (in the horizontal direction) were typically smaller than the size of the dots.

errors) versus the determined thicknesses (in units of Λ) is shown in Figure 2.7.

A qualitative explanation of these results may lie in the fact that the optical properties of evaporated carbon depend markedly on the conditions of preparation[56]. Thus, the fitted Drude function constants of Eq. 2.3 determined by Ashley[45] may not accurately apply to the evaporated carbon produced by Arizona Carbon Foil Company. This could explain the relatively good agreement of Ashley's Λ with the results of Lencinas *et al.*[44] (who obtained carbon targets from a source other than Arizona[57]), but relatively poor agreement with other measurements taken at lower energies.[58,59] For this measurement, the thinner foils for which energy loss data was taken have been calibrated using Λ= 42 a.u.. The determined thicknesses (for targets $< 5\ \mu g/cm^2$) are given in Table 2.2. For the thicker foils, the manufacturer's claimed thicknesses were used.

Table 2.2: Table of determined thicknesses of carbon foils used in the convoy electron measurement.

Manufacturer ($\mu g/cm^2$)	Fit Results ($\mu g/cm^2$)
0.5	1.0
0.5	1.2
1.0	1.4
1.5	1.8
2.6	2.2
3.5	3.5
4.1	3.8
4.9	5.3

2.3 Data Collection and Storage

Shown in Figure 2.8 is a block diagram of the electronics set-up for data acquisition and storage. The system was controlled by a Compaq 386s computer, running a histogramming software program[60] designed to acquire, display and store the data. During data acquisition, the program was interrupted by event signals on either of two MetraByte model PI012 interface cards. In this experiment, an event was defined as either the detection of an electron on the PSD, or the completion of a preset dose of ion beam current (detected by the Faraday cup).

In case of a PSD event, the 16-bit combined x and y digital position information from the position decoder and the 12-bit digital "energy" (E) information (i.e. DAC input used for programming the spherical spectrometer's voltage) were used as the indices of a three-dimensional histogram. In the program, the indices were combined so as to define an address in memory where the number of events were stored corresponding to a given combination of x, y, and E. In order to store all the information in the available memory, the precision of these quantities was reduced to 6 bits (64 channels) for x, 3 bits (8 channels) for y and 7 bits (128 channels) of energy. For this experiment, the x-direction corresponded to the direction of the plane perpendicular to the spherical sector analyzer's deflection plane. More precision was saved for this direction since the analyzer's focussing properties were better in this plane. Allowing two bytes for each channel in the array (x, y, E) for a maximum of $2^{16} - 1$ or 65535 counts in each channel required a total of 128 Kbytes of memory.

In the case of a "dose-completion" event, the digital DAC input was changed to correspond to the next desired deflection voltage, and a small delay was added to compensate for the finite slew-rate of the sector power supplies. The dose electronics were set so that about one second was spent at any particular energy channel

Figure 2.8: Block diagram of the electronics set-up. (A) Anode signals from the PSD are amplified and sent to the position decoder for conversion into digital position information. Either a strobe signal sent by the position decoder or an external busy input sets a system busy output on an electron event interface module. This is used to gate off the current integration during computer dead time. (B) The current signal from Faraday cup is sent to a current digitizer which sends a pulse to a counter after collecting 100 picoCoulombs of charge. When the counter reaches a predetermined setting, a dose completion signal is sent to the dose event interface module. If either a dose completion or a electron event signal is received by the interface modules, an interrupt signal is sent to the corresponding parallel port interface card placed in the Compaq 386s computer. Upon receiving a dose event, the computer increments the input to a digital-to-analog converter (DAC). Upon receiving an electron event, the computer increments a register located at an memory address defined by the digital position and energy information of the event. (C) The DAC controls the programmable power supplies which provide the desired voltage to the spectrometer sectors.

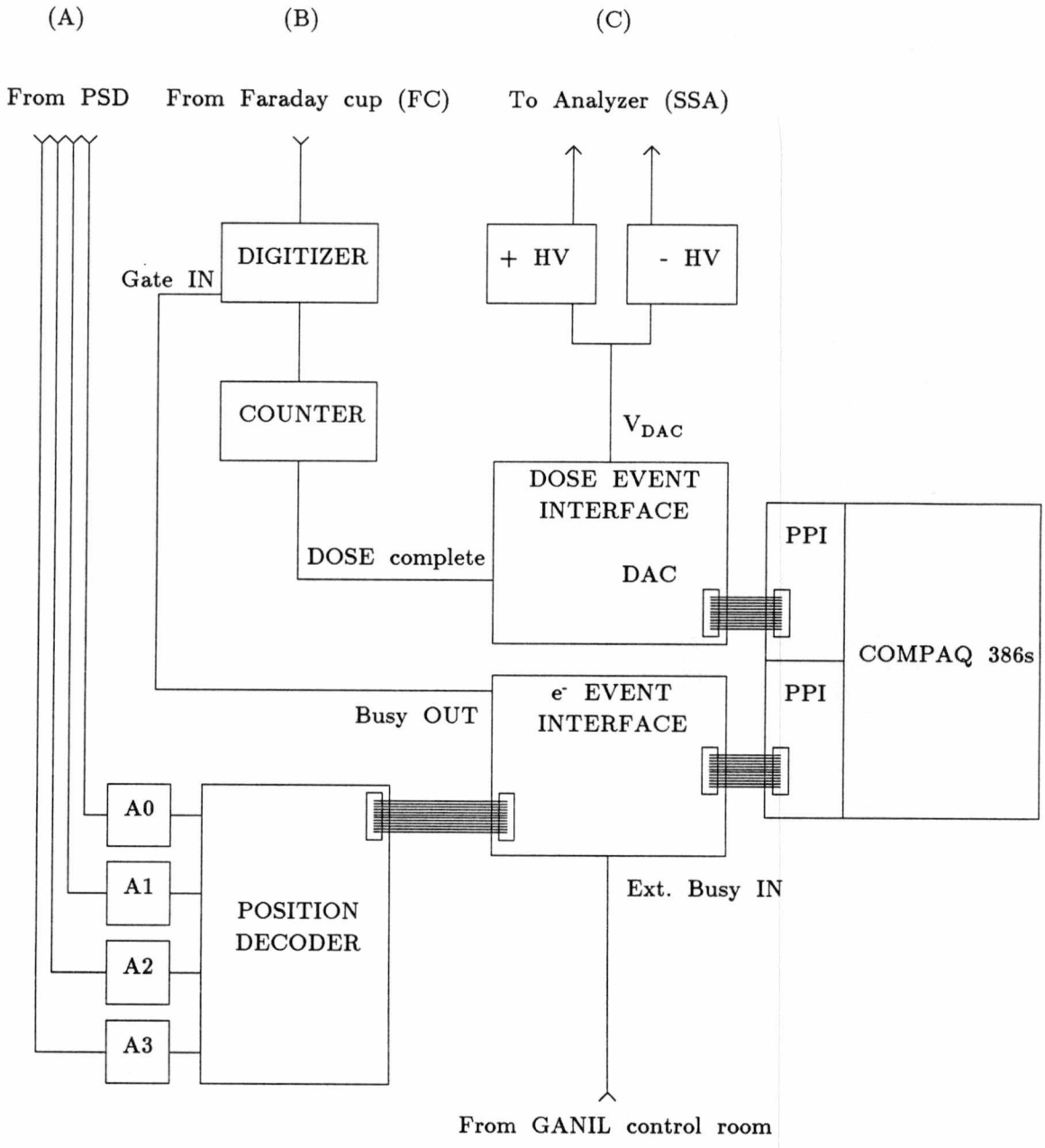
(A)
(B)
(C)
From PSD
From Faraday cup (FC)
To Analyzer (SSA)
DIGITIZER
Gate IN
+ HV
- HV
COUNTER
V_{DAC}
DOSE EVENT
INTERFACE
DAC
DOSE complete
PPI
COMPAQ 386s
PPI
e⁻ EVENT
INTERFACE
Busy OUT
A0
A1
A2
A3
POSITION
DECODER
Ext. Busy IN
From GANIL control room

making the time required for a full 128-channel scan approximately two minutes. A typical dataset was comprised of about 30 scans and took around one hour to complete.

Chapter 3

DATA REDUCTION AND ANALYSIS

3.1 Extraction of Spectra

3.1.1 Method of Reduction

In order to analyze the data, it was necessary to convert the set into a more suitable form for extraction of multipoles. As was discussed in the previous chapter, the data acquisition system allowed determination of the lab-frame electron emission angles θ_e ($\leq 4°$) and ϕ_e, as well as the lab-frame energy E_e. Unfortunately, the memory restrictions of the data acquisition computer do not allow for a complete three-dimensional histogram of these parameters. However the ϕ_e variable is not important here, since the collision has azimuthal symmetry about the projectile velocity $\vec{v}_p$. This data were therefore reduced to two dimensions by saving only the polar angle information (i.e. θ_e) for those events occurring within a particular "azimuthal slice" of the PSD.

First, it was necessary to determine the PSD "center", or the (x, y) position (see Figure 2.5) on the PSD where $\theta_e = 0°$. This was accomplished by measuring a full high-resolution image at a spectrometer pass energy corresponding to the matching

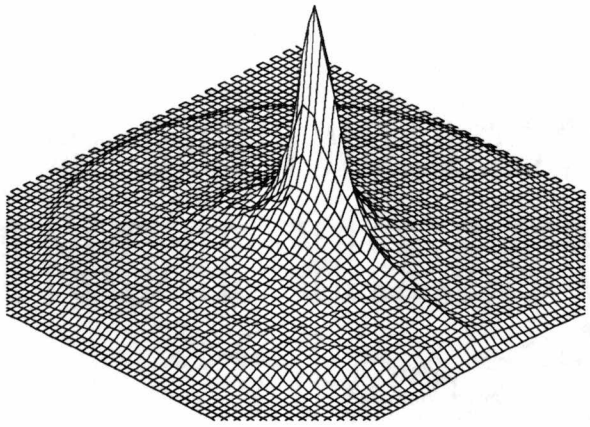

Figure 3.1: Image of convoy electron angular distribution on PSD at velocity $v_e = v_p$.

velocity $\vec{v}_e = \vec{v}_p$. At this velocity the v_e^{-1} singularity of the differential cross section reduces (non-relativistically) to $(1 - \cos\theta_e)^{-1/2}$. While the finite angular resolution element of the spectrometer and PSD removes this polar angle singularity, the angular emission at this energy is still sharply peaked, as demonstrated by a typical PSD image displayed isometrically in Figure 3.1.

The orientation of the slice (or the azimuthal angles ϕ_e and $\phi_e + \pi$ at which it is positioned) is determined from the orientation of the spectrometer. Since the 160° spectrometer focuses better in the plane perpendicular to the plane of dispersion, this direction was chosen for the slice. Strictly speaking, the slice is not azimuthal, since its boundaries lie along constant y (as defined by the PSD electronics) and not constant ϕ_e. As a result, larger polar angles have a smaller azimuthal contribution in the generated two-dimensional spectra. This effect is accounted for in the data fitting routine (see Section 3.2).

For the small polar angles considered here, $\theta_e \sim \tan\theta_e$, so that θ_e is proportional to the radial distance from the center (0°) of the PSD. Thus, the PSD's x direction along the slice is directly proportional to the angle θ_e. Since 0° is usually near the

physical center of the PSD, $\theta_e(x)$ ranges from around 4° to 0° (at ϕ_e) and back to 4° (at $\phi_e + \pi$). The PSD electronics subdivide both the x and y directions into 64 equally spaced channels, giving a total of 4096 pixels. The angular data were reduced to a single dimension by summing (for each of the 64 x channels) the 8 y channels located within the slice along constant y. This information is recorded for each of 64 equally spaced spectrometer pass energies giving a final two-dimensional matrix (64 × 64 channels) representing the distribution in energy and polar emission angle of the convoy electrons.

A sample of the results for the incident Argon ion beams are displayed in the following three figures. Plotted are contours of equal emission intensity representing multiples of 12.5% of the peak height. While the data are displayed in energy and angle space, the relative scaling between vertical and horizontal axes is chosen so that the corresponding parallel and perpendicular projectile-frame velocity intervals, $\Delta v_{\|}$ and $\Delta v_{\perp}$, are equal. Using the Einstein velocity addition rules (see Eq. A.6) the relations

$$\begin{aligned} \Delta v_{\perp} &= \Delta(v_e \sin\vartheta_e) \sim \gamma \mathrm{v_p} \Delta\theta_e \\ \Delta v_{\|} &= \Delta(v_e \cos\vartheta_e) \sim \Delta \mathrm{v_e} \sim \frac{\Delta \mathrm{E_e}}{\mathrm{v_p}} \end{aligned} \tag{3.1}$$

can be derived which determine the axis scaling factors.

3.1.2 Emission Distributions

In this section, emission distributions observed during the course of the experiment are presented to provide an overview of some of the issues that must be addressed by the analysis. In Figure 3.2, contours of distributions from incident Ar^{15+} are displayed. The distributions are plotted in order of increasing target thickness to best view the shape evolution with projectile dwell time in the solid. Also plotted are data taken from incident 82 MeV O^{5+} (v_p =14 a.u.) + Ar. These data, taken under single collision conditions (SCC), are displayed next to the thinnest target

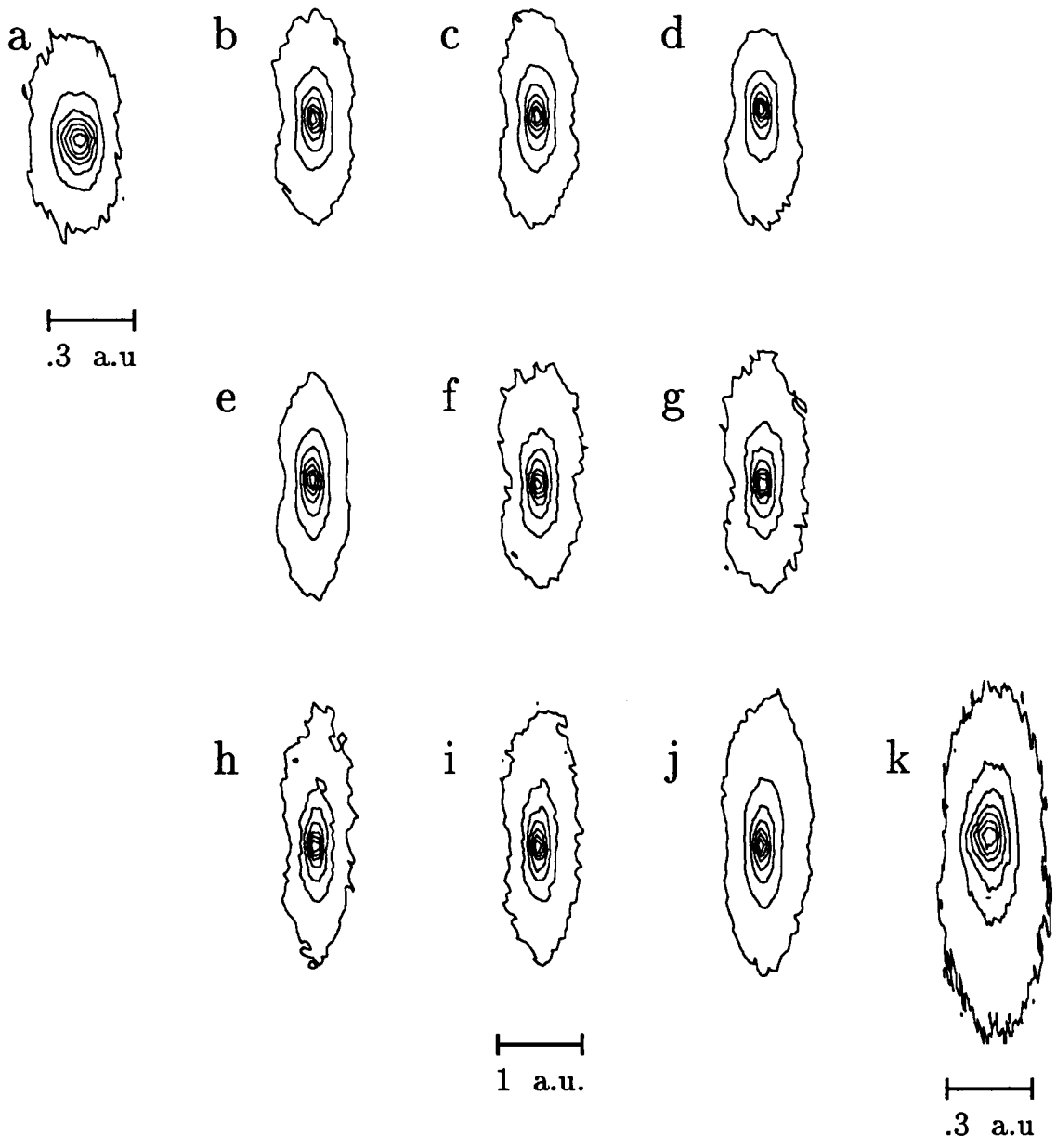

Figure 3.2: Contours of electron emission distributions for v_p=37 a.u. Ar^{15+} in C, and O^{5+} in Ar (v_p=14 a.u.) and C (v_p=17 a.u.). Projectile-frame velocity scales are displayed. (a) O^{5+} + Ar. (b)–(j) Ar^{15+} + C, ρx = (b) 0.5 $\mu g/cm^2$. (c) 1.5 $\mu g/cm^2$. (d) 2.6 $\mu g/cm^2$. (e) 3.5 $\mu g/cm^2$. (f) 4.1 $\mu g/cm^2$. (g) 4.9 $\mu g/cm^2$. (h) 8.0 $\mu g/cm^2$. (i) 10.1 $\mu g/cm^2$. (j) 21.4 $\mu g/cm^2$. (k) O^{5+} + C, ρx = 0.5 $\mu g/cm^2$.

data for comparison. As is evident from the figure, these data appear to have very similar angular emission distributions.

It is important to note that while the velocity, projectile and target charge are all different in the above-mentioned ion-atom collision system, both collision systems still have important similarities. First, both projectiles are Li-like ($1s^22s$) and detected near-threshold electrons are produced primarily from ELC of the valence electron. Secondly, the ratio of the orbital velocity of the electron's initial state v_{orb} to the projectile velocity v_p in both cases is about 1/4. As pointed out in Eq. 1.4, the small ratio is necessary for the application of the first-Born approximation of Burgdörfer[31] which predicts a projectile-frame differential cross section of the form,

$$\frac{d^2\sigma}{dE_e d\Omega_e} = \sigma_0 \sum_{j=0} v_e^{j-1}(\beta_{j,0} + \beta_{j,2}P_2(\cos\vartheta_e) + \beta_{j,4}P_4(\cos\vartheta_e)), \qquad (3.2)$$

for ELC of the n=2 electron. Furthermore, theoretical calculations of the magnitude of the asymmetry coefficients $\beta_{0,k}$ by Burgdörfer have found no significant dependence on either the projectile or target charge Z_p, Z_T.[62] The qualitative agreement between the ion-atom and thin ion-solid data pictured in Figure 3.2 supports these arguments.

In contrast to the thin target data, the data for thicker targets indicate an even stronger preference for transverse emission. This increased transversality is in agreement with the results of previous convoy electron data[8,63,66] taken under plural collision conditions. These past results have also been characterized by high-order multipole content, signifying the contribution of ELC from high n-states ($n \sim 5$). For comparison, data from the collision system O^{5+} (v_p = 17 a.u.) + 0.5 $\mu g/cm^2$ C are also displayed. (It is important to recall that this lower velocity system demonstrated no significant target thickness-dependence of the angular distributions—the choice of the relatively thin 0.5 $\mu g/cm^2$ C-foil is somewhat arbitrary.) It is clear that the angular shape of the lower velocity convoy electron data agrees qualitatively with the thicker target Ar^{15+} data. Thus the distributions displayed here

indicate an evolution of convoy electron angular emission to a strongly transverse "equilibrium".

In Figure 3.3, contours of distributions from incident Ar^{17+} are displayed, plotted in order of increasing target thickness. As is evident from these data, there is a pronounced change in emission shape over a relatively small range of foil thicknesses. Surprisingly, the thinner target data contain contain primarily *odd-order* multipoles as is evident in their longitudinal (or "forward-backward") asymmetry, usually seen only for ECC cusps. However, it is unlikely that ECC events are responsible for this behavior in the data: the number of convoy electrons produced per incident ion for incident (bare) Ar^{18+} is about 50 times lower than the number produced for incident Ar^{17+} . Since the ECC probability for these two ions should not change significantly, the enhancement of the convoy yield for incident (hydrogenic) Ar^{17+} must be due to ELC. Thus the contribution of ECC to these data for incident Ar^{17+} is less than 2%.

The presence of longitudinal asymmetries is more likely due to the failure of the first-Born approximation for this system. In this case, the mean orbital velocity for the ground-state ($1s$) electron is $\sim$ 18 a.u.—only about half the projectile velocity. In a recent second-Born approximation calculation for ELC, Jakubaßa-Admundsen[61] has found similar results in the emission distributions for He^+ ($v_{\rm orb} \sim 2$ a.u.) + He at $v_p \leq 4$ a.u. (i.e. $v_{\rm orb}/v_{\rm p} \sim 1/2$). A more quantitative comparison between the present data and the results of Jakubaßa-Admundsen, involving the odd-order asymmetry coefficients, is made in the following section.

For thicker targets, the Ar^{17+} distributions become more transverse and begin to lose their longitudinal asymmetry—both characteristics of ELC from higher n-states. Therefore these data suggest the increasing presence of excited state contributions to the convoy yield for these targets. Furthermore, the thicker targets appear to have angular distributions similar to the thick target data of Ar^{15+} . This implies that the angular distribution equilibrium is independent of projectile charge

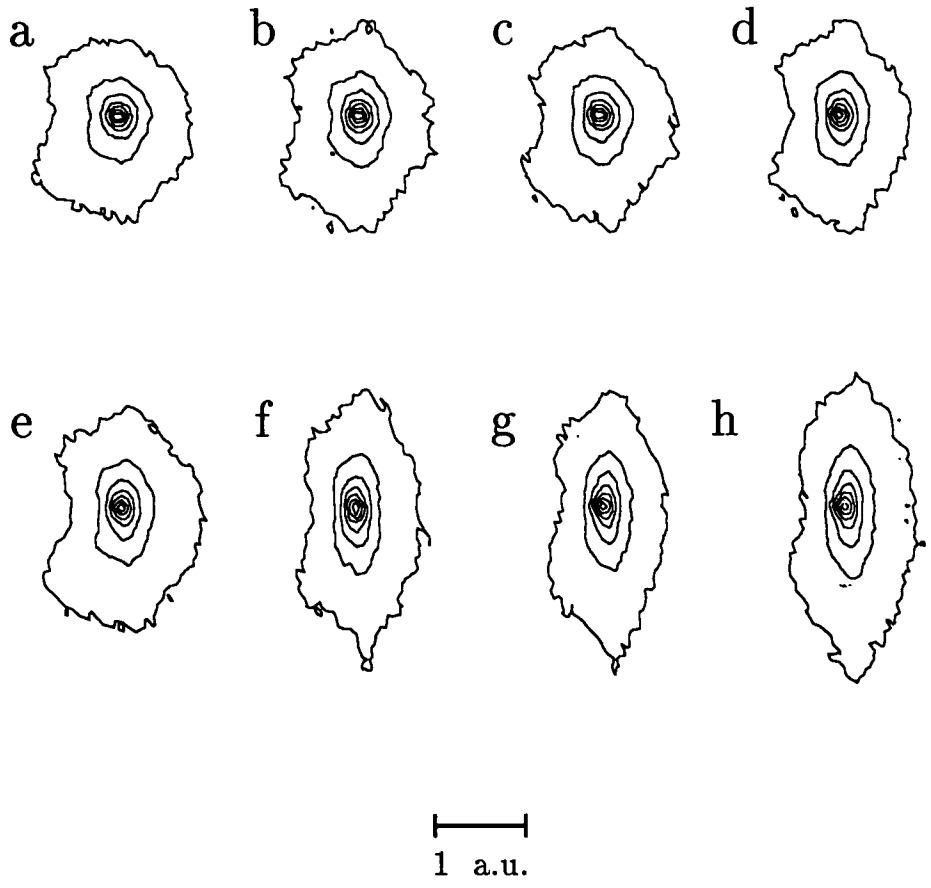

Figure 3.3: Contours of electron emission distributions for v_p=37 a.u. Ar^{17+} incident on carbon foils. (a)–(h) Ar^{17+} + C, ρx = (a) 1.0 $\mu g/cm^2$. (b) 1.5 $\mu g/cm^2$. (c) 2.6 $\mu g/cm^2$. (d) 3.5 $\mu g/cm^2$. (e) 4.9 $\mu g/cm^2$. (f) 8.0 $\mu g/cm^2$. (g) 10.1 $\mu g/cm^2$. (h) 21.4 $\mu g/cm^2$.

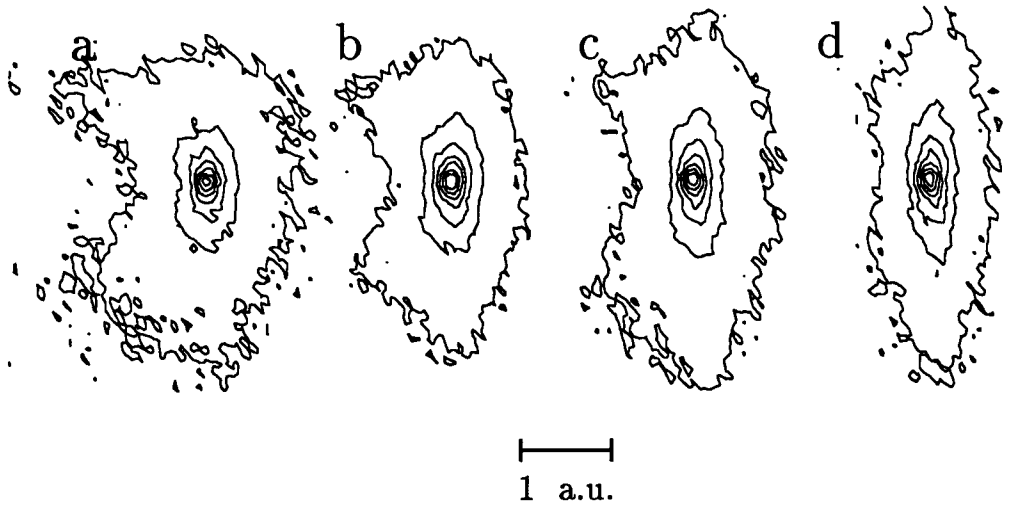

Figure 3.4: Contours of electron emission distributions for v_p=37 a.u. Ar^{18+} incident on carbon foils. (a)–(d) Ar^{18+} + C, ρx = (a) 3.5 $\mu g/cm^2$. (b) 4.9 $\mu g/cm^2$. (c) 10.1 $\mu g/cm^2$. (d) 21.4 $\mu g/cm^2$.

Z_p.

Pictured in Figure 3.4 are the resulting distributions for incident bare Ar^{18+} projectiles. As pointed out previously, the experimental convoy yield for this system was relatively low, making the time necessary to acquire a dataset with good statistics rather long. As a result, only four different thicknesses were measured. The measured data become increasingly transverse with increasing target thickness, as did the previous spectra. Furthermore, there appears to be some longitudinal asymmetry present as well.

Unlike the collisions involving incident Ar^{15+} and Ar^{17+} , the primary processes responsible for convoy production with incident Ar^{18+} are unclear. In competition with ECC (the SCC-process) is a two-step mechanism involving the capture of a target electron into a bound state followed by a rapid ELC process. The so-called ECLC process (Electron Capture-Loss to the Continuum) has been previously suggested to explain the longitudinal symmetry of singly-differential convoy distri-

butions produced by bare incident ions.[27,63] Additionally, ECC is not expected to produce significant multipole moments higher than β_1[64]. Thus, the tranverse distributions pictured here probably indicate the presence of ECLC in this data.

3.2 Multipole Moment Determination

3.2.1 Transformation and Convolution of the Differential Cross Section

In order to quantitatively compare the observed distributions with theoretical predictions of ion-atom ELC and ECC processes as well as with other experimental studies of both cusp and convoy electrons, the data were fit to the multipole expansion discussed in Chapter 1 (i.e. Eq. 1.2). Modifications to this form of the lab-frame doubly-differential cross section (DDCS) were necessary to account for the small but finite relativistic effects present in this measurement. This form must also be convoluted with the finite experimental resolution of the experimental apparatus.

Using an approximate form of the Einstein velocity addition rules, the relativistic lab-frame DDCS for near-threshold continuum electrons is shown in Appendix A to be

$$\frac{\mathrm{d}^2\sigma}{\mathrm{dE_e d\Omega_e}} = \gamma \mathrm{v_e} \sigma_0 \sum_{j,k} \beta_{j,k} v_e^{j-1} P_k(\cos\vartheta_e), \tag{3.3}$$

where v_e and ϑ_e are the electron velocity and polar emission angle in the projectile-frame, and γ is the relativistic correction factor associated with the projectile velocity $\mathrm{v_p}$,

$$\gamma \equiv \frac{1}{\sqrt{1-\beta^2}}$$
$$\beta \equiv \frac{\mathrm{v_p}}{c}. \tag{3.4}$$

The observed data is described by integrating the DDCS over the experimental resolution. Following the line of earlier work[28,65], the resolution function has been

approximated as being separable in energy and angle. The observed distribution in the lab-frame may then be written

$$I(\mathrm{E_e},\theta_e) = \int_{\Delta\Omega_e} \mathrm{d}\Omega_e' G(\Omega_e,\Omega_e') \int_{\Delta \mathrm{E_e}} S(\mathrm{E_e},\mathrm{E_e}')\mathrm{dE_e}' \frac{\mathrm{d}^2\sigma}{\mathrm{dE_e}'\mathrm{d}\Omega_e'}(\mathrm{E_e}',\Omega_e'), \qquad (3.5)$$

where $G(\Omega_e,\Omega_e')$ and $S(\mathrm{E_e},\mathrm{E_e}')$ represent the angle and energy resolution functions respectively. The energy resolution function has been described previously[28,65] as being approximately of a trapezoidal shape, with a full-width at half-maximum (FWHM) proportional to the resolution $\delta\mathrm{E}/\mathrm{E}$ and a top-width proportional to the difference in entrance and exit apertures of the spectrometer.[40] For spectrometers with rectangular entrance and exit apertures, the resolution has been written:

$$\frac{\delta \mathrm{E}}{\mathrm{E}} = \frac{a_1 + a_2}{2r} \qquad (3.6)$$

where a_1, a_2 are the entrance and exit aperture radii respectively, and r is the radius of curvature of the mean trajectory in the spectrometer. In this experiment the exit aperture was 1.5 mm diameter. There was no fixed entrance aperture so that a_1 was determined by the size of the ion beam at the entrance focus of the spherical sector spectrometer. The focussing elements prior to and in LISE were set to provide a 1.0 mm diameter beam at the spectrometer's entrance focus. Using the spectrometer radius of curvature, r =55 mm, the resolution given by Eq. 3.6 is found to be about .011.

The angular resolution function, $G(\Omega_e,\Omega_e')$, is primarily due to the finite size of the spectrometer's exit aperture a_2. Assuming that the distribution of electrons exiting the spectrometer uniformly illuminate the exit aperture, electrons exiting the spectrometer with a particular angle (with respect to the central ray) will uniformly strike an area on the PSD the size of the exit aperture. Thus, the resolution function has been assumed to have a "pillbox" shape[65,33]; i.e. unity over an area the size of the exit aperture and zero everywhere else. The corresponding angular uncertainty $\delta\theta_e$ becomes

$$\delta\theta = \frac{a_2}{l} \qquad (3.7)$$

where l is the distance traveled by the electron in the drift region following the exit aperture. Using l =150 mm for this experiment, the angular resolution $\delta\theta$ is found to be 5 mrad. It should be stressed that this geometric determination of $\delta\theta$ ignores the effects of spectrometer angular abberations and fringe fields. Thus, this equation for $\delta\theta$ should be regarded as an approximation, or at worst, a lower limit on the value of $\delta\theta$.

Since the integrals in Eq. 3.5 are done in the laboratory frame while the DDCS is expressed in projectile-frame variables, a relativistic tranformation must be made to write v_e and ϑ_e in terms of the variables of integration. The details of this derivation are shown in Appendix B. Substituting the dimensionless variables $\rho = \mathrm{v_e}/\mathrm{v_p}$ and $z = v_e/\mathrm{v_p}$, the resulting intensity can be written

$$I(\mathrm{E_e}, \theta_\mathrm{e}) \approx \frac{\mathrm{v_e}\sigma_0}{\gamma} \int_{\Delta \mathrm{E_e}} \mathrm{dE'} S(\mathrm{E_e}, \mathrm{E_e}') \frac{2g\Delta\phi_\mathrm{e}(z_1)}{1+\beta^2 f} \sum_{n,k} \beta_{j,k} {\mathrm{v_p}}^n \int_{z_1}^{z_2} dz z^n P_k(\frac{f}{z} + gz), \quad (3.8)$$

where $\Delta\phi_\mathrm{e}(z)$ is the θ_e-, or z-dependent azimuthal range of the resolution function obtained by integration over ϕ_e. The functions f and g are defined as

$$\begin{aligned} f(\rho,\gamma) &= \frac{\rho^2-1}{2}\left(1+\frac{\beta^2(\rho^2-1)}{4}\right) \\ g(\rho,\gamma) &= \frac{-1}{2\gamma^2}\left(1+\frac{\beta^2(\rho^2-1)}{2}\right). \end{aligned} \quad (3.9)$$

If the azimuthal slice width w is sufficienty larger than the angular resolution pillbox, it is necessary to integrate the intensity in the PSD's y direction. It is easily seen that the final experimental intensity becomes

$$I^{\mathrm{exp}}(\mathrm{E_e}, \theta_\mathrm{e}) = 2\int_0^{\frac{w}{2}} I(\mathrm{E_e}, \theta_\mathrm{e}(\sqrt{x^2+y^2}))dy. \quad (3.10)$$

Since the argument of the Legendre polynomial in Eq. 3.8 must be raised to the k^{th} power, it is is useful to write

$$
\begin{aligned}
x &\equiv \frac{f}{z} + gz \\
x^2 &= \frac{f^2}{z^2} + 2fg + g^2z^2 \\
&\vdots \quad \vdots \\
x^n &= \sum_{i=0}^{n} {}_nC_i \left(\frac{f}{z}\right)^i (gz)^{n-i}; \qquad {}_nC_i \equiv \frac{n!}{i!(n-i)!.}
\end{aligned} \tag{3.11}
$$

Defining the coefficient of x^j in the Legendre polynomial $P_k(x)$ as $COEF(k,j)$, the integral over z becomes

$$
\int z^n P_k(x) dz = \sum_{j=0}^{k} COEF(k,j) \sum_{i=0}^{j} {}_iC_j f^i g^{j-i} \times
\begin{cases}
\frac{z^u}{u} & \text{if } u \equiv n+j-2i+1 \neq 0 \\
\ln z & \text{otherwise}
\end{cases} \tag{3.12}
$$

This equation suggests the method used to evaluate Eq. 3.8. After initially determining the Legendre coefficients using a recursion relation, the energy integration is done numerically. At each energy point within the integration, the matrix $FG(i,j)$, whose components are ${}_iC_j f^i g^{j-i}$, is created and used to analytically evaluate the angular integrations for each k and n desired. This method allows for rapid evaluation of the double integral—a typical 64 by 64 channel spectrum takes approximately 2 minutes to generate on a MicroVax II computer.

A number of generated distributions, contoured as described earlier, is shown in Figure 3.5. The resolution values determined above (δE/E = 0.011, $\delta\theta$ =5 mrad) were used in the convolution. Each contour plot represents the resulting distribution when a particular $\beta_{0,k}$ ($k = 1-6, 8, 10$) is set to (-1) and combined with the isotropic term $\beta_{0,0} = 1$.

3.2.2 Fit of Experimental Data

Extraction of multipoles is made by utilizing a non-linear least squares fit[49] of a spectral data set to Eqs. 3.10 and 3.8. There were 18 adjustable parameters in

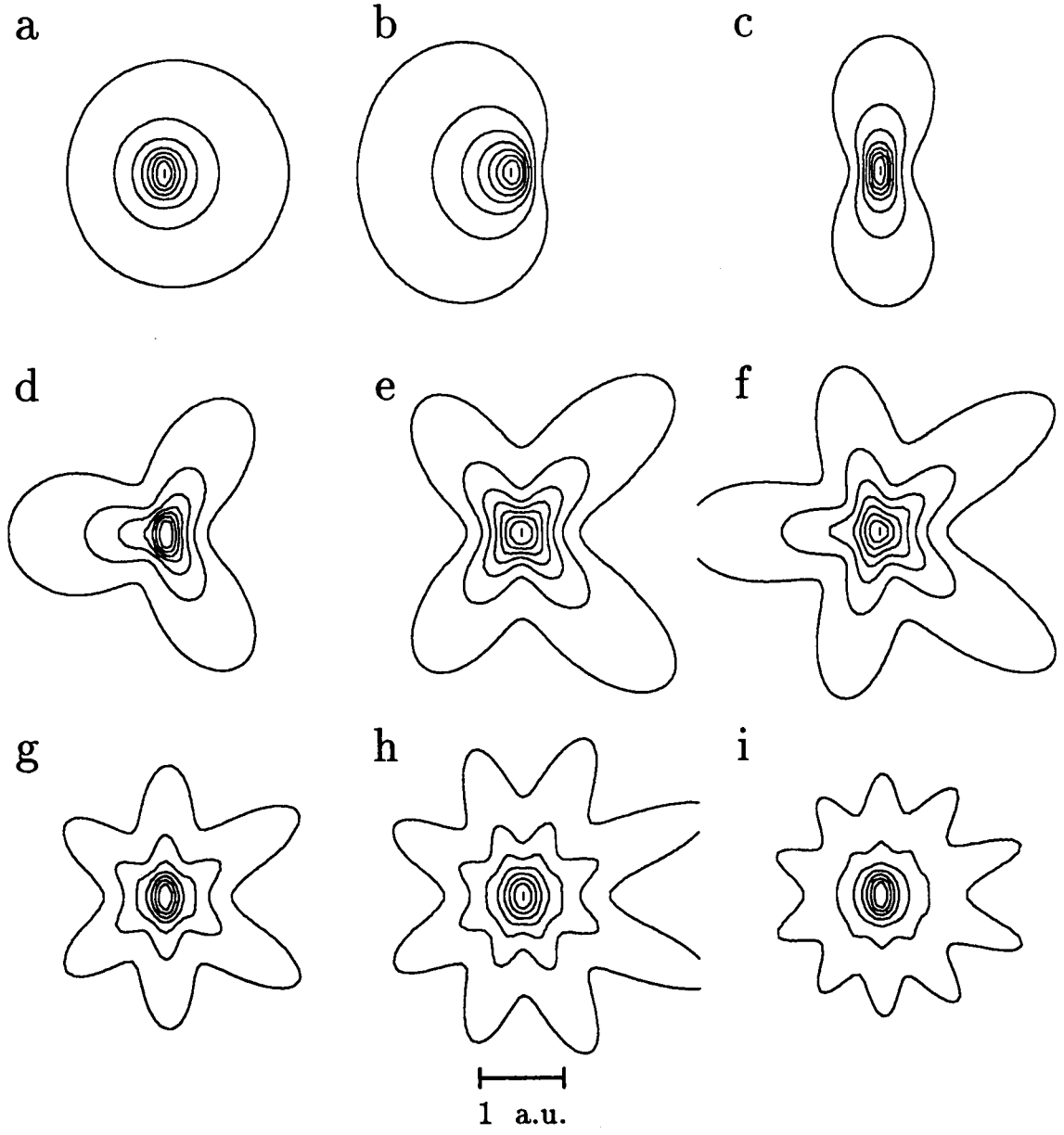

Figure 3.5: Contours of generated multipole distributions. (a) $\beta_{0,0}$ only. (b)–(i) $\beta_{0,0} = 1, \beta_{0,k} = -1$ (b) k=1. (c) k=2. (d) k=3. (e) k=4. (f) k=5. (g) k=6. (h) k=8. (i) k=10.

the fit: 14 $\beta_{j,k}$'s, two parameters to locate the center channel ($\theta_e = 0°, \mathrm{E_e} = \mathrm{E_{cusp}}$), one parameter to characterize the approximately linear relative efficiency of the microchannel plate[33], and the cross section amplitude σ_0. The range of energies and angles fit was chosen (as closely as possible) to correspond to a range of $\pm$ 1.0 a.u. in $v_{||}$ and $v_{\perp}$. Furthermore, the region at the matching velocity corresponding to a resolution volume was eliminated from the fit: the spectra are dominated in this area by the v_e^{-1} singularity convoluted with the resolution function which is in turn dominated by $G(\Omega_e, \Omega_e')$ and $S(\mathrm{E_e}, \mathrm{E_e}')$ rather than by the DDCS. This step was taken to avoid uncertainties in the resolution functions significantly influencing the fitted results.

Errors in $\beta_{j,k}$ due to uncertainties in the energy and angular resolution were estimated by changing the resolution parameters by one error bar and refitting the data. The uncertainties in $\delta\theta$ ($\pm$ 4 mrad) and δE ($\pm$ 0.1% of E) were estimated by comparing the results of Eq. 3.6 and Eq. 3.7 with the results obtained from a Monte Carlo simulation of this spectrometer.[41] The changes in the refitted $\beta_{j,k}$'s were generally smaller (by about a factor of four) than the corresponding uncertainties in $\beta_{j,k}$ associated with the fit itself. These two sources of errors were added in quadrature to obtain the final error in $\beta_{j,k}$.

The number of $\beta_{j,k}$'s needed to fit the data was determined only after many early fitting attempts. The decision involved both the number of angular moments k and radial velocity corrections n.

For the angular component it was found that the thicker targets contain significant even order multipole moments $\beta_{j,k}$'s up to $\beta_{0,10}$. This result is in agreement with previous measurements at lower velocites.[8,66] Beyond k=10, the relative errors in fitted $\beta_{j,k}$ become large enough to cast strong doubts on their statistical significance. Still, there does appear to be a trend of $\beta_{0,10}$ with increasing target thickness.

Since the presence of odd order contributions in the data (particularly high order

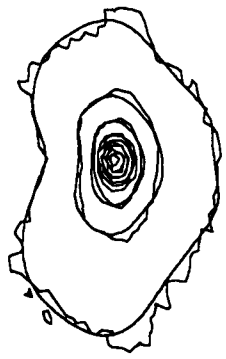

Figure 3.6: Overlay of fit including only β_1 and β_3.

odd terms) was somewhat of a surprise, it was impossible to draw from experience the number of odd-k $\beta_{j,k}$'s to fit. Initially it appeared as though there were only single- and triple-lobed shapes in the Ar^{17+} and Ar^{18+} data, but it became clear later that an additional term was required. An example is shown in Figure 3.6 where we have overlaid a fit including only the odd order terms $\beta_{j,1}$ and $\beta_{j,3}$ to the corresponding dataset generated from Ar^{17+} + 3.5 $\mu g/cm^2$C. As demonstrated in the figure, there exists five areas approximately equally spaced ($\sim 72°$ apart) where the fit deviates slightly from the experimental data, suggesting the need to add a $\beta_{j,5}$-parameter to the fit.

Only the first order radial velocity component terms (j=0) were fitted to the data initially. The main incentive for this was that there exists theoretical predictions only for these terms. Furthermore, selecting a projectile-frame velocity range < 1 a.u. should cause the fit to be dominated by the "singular data" at the matching velocity. However, at this high projectile velocity the resolution volume $\delta v_{||}(\delta v_{\perp})^2$ becomes large since it is proportional to the electron velocity squared. Thus a larger range of channels had to be fit ($\Delta v_{||} \sim \Delta v_{\perp} \sim 1$ a.u.) in order to extract the an-

gular information not dominated by the singularity-convoluted-with-the-resolution functions. In order to adequately fit this range, it was necessary to add the first order terms $\beta_{1,k}$, $k < 6$.

Although adding these second order velocity correction terms significantly lowered the χ^2 of the fit, it also presented a problem for comparison with theoretical predictions of the multipole content. Since the range of v_e's fit were all close to 1 a.u., it was decided to define an effective multipole moment, β_k, where

$$\beta_k \equiv \beta_{0,k} + < v_e > \beta_{1,k}$$
$$(< v_e > \approx 1\text{a.u.}), \tag{3.13}$$

where $< v_e >$ is the value of the projectile-frame emission velocity averaged over the region of the fit. It is important to note that this procedure was attempted only because the range of projectile-frame velocities fitted was small: The large resolution volume which was eliminated from the fit contained most of the region where $v_e \ll 1$. In such a case, it is easily seen that the first two terms of the velocity expansion of the projectile-frame DDCS reduce to

$$\frac{d^2\sigma}{dE_e d\Omega_e} \rightarrow \sigma_0 \sum_k \beta_k P_k(\cos\theta_e), \tag{3.14}$$

where β_k is defined in Eq. 3.13. The resulting β_k's agreed well (within 20%) with the previously-fitted $\beta_{0,k}$'s. Furthermore, the addition of the first-order velocity correction terms allowed us to generate results to compare with theoretical predictions of multipolarity without compromising on the goodness of the fit. The results of these fits are summarized in Tables 3.1 and 3.2.

Table 3.1: Table of fitted even-order effective β_k's. Errors determined are given in parentheses.

Projectile	Target Thickness ($\mu g/cm^2$)	β_2	β_4	β_6	β_8	β_{10}
Ar^{17+}	1.4	-.09(.02)	.01(.03)	-.11(.01)	.01(.01)	-.04(.01)
"	1.8	-.18(.03)	.02(.04)	-.16(.01)	.02(.01)	-.08(.01)
"	2.2	-.18(.02)	.00(.03)	-.14(.01)	.02(.01)	-.03(.01)
"	3.5	-.32(.02)	.04(.03)	-.13(.01)	.05(.01)	-.08(.02)
"	5.3	-.32(.02)	.01(.03)	-.10(.01)	.05(.01)	-.01(.01)
"	8.0	-.54(.01)	.17(.02)	-.15(.01)	.06(.01)	-.07(.02)
"	10.1	-.59(.02)	.22(.03)	-.16(.01)	.09(.01)	-.07(.02)
"	21.4	-.67(.02)	.27(.03)	-.16(.01)	.07(.01)	-.05(.02)
Ar^{18+}	3.5	-.48(.06)	.08(.10)	-.14(.03)	.12(.03)	.02(.04)
"	5.3	-.51(.04)	.06(.05)	-.10(.01)	.09(.02)	-.01(.02)
"	10.1	-.64(.04)	.20(.06)	-.16(.02)	.08(.02)	-.03(.03)
"	21.4	-.75(.05)	.29(.08)	-.25(.02)	.11(.02)	-.09(.04)
Ar^{15+}	1.0	-.76(.02)	.27(.03)	-.13(.01)	.04(.01)	-.06(.02)
"	1.8	-.77(.02)	.29(.03)	-.16(.01)	.08(.01)	-.06(.02)
"	2.2	-.80(.01)	.29(.05)	-.12(.01)	.05(.01)	-.06(.02)
"	3.5	-.83(.01)	.38(.01)	-.24(.01)	.13(.01)	-.12(.03)
"	3.8	-.78(.04)	.29(.05)	-.15(.02)	.08(.02)	-.02(.02)
"	5.3	-.84(.04)	.34(.05)	-.19(.01)	.06(.02)	-.05(.02)
"	8.0	-.94(.05)	.50(.06)	-.33(.02)	.22(.02)	-.12(.03)
"	10.1	-.91(.04)	.47(.05)	-.30(.02)	.16(.02)	-.11(.04)
"	21.4	-.93(.01)	.48(.05)	-.30(.01)	.16(.01)	-.11(.02)

Table 3.2: Table of fitted odd-order effective β_k's. Errors determined are given in parentheses. χ^2_ν results from all even and odd terms listed in tables.

Projectile	Target Thickness ($\mu g/cm^2$)	β_1	β_3	β_5	χ^2_ν
Ar^{17+}	1.4	-.20(.02)	.09(.02)	.09(.04)	1.2
"	1.8	-.16(.02)	.10(.05)	.09(.05)	1.1
"	2.2	-.14(.02)	.12(.02)	.10(.04)	1.2
"	3.5	-.12(.02)	.15(.02)	.10(.03)	1.4
"	5.3	-.06(.02)	.15(.02)	.10(.04)	1.4
"	8.0	.01(.01)	.12(.02)	.08(.02)	1.9
"	10.1	-.02(.02)	.10(.03)	.07(.04)	1.6
"	21.4	.09(.02)	-.02(.03)	.12(.04)	1.5
Ar^{18+}	3.5	-.23(.06)	.15(.08)	.09(.11)	1.1
"	5.3	-.13(.03)	.11(.05)	.08(.07)	1.1
"	10.1	-.04(.03)	.02(.06)	.07(.08)	1.1
"	21.4	-.02(.04)	-.05(.07)	.11(.10)	1.1
Ar^{15+}	1.0	-.05(.02)	.09(.03)	-.02(.04)	1.3
"	1.8	-.02(.02)	.07(.03)	-.02(.04)	1.5
"	2.2	.01(.02)	.05(.03)	.00(.01)	2.0
"	3.5	.00(.01)	.09(.08)	-.01(.01)	1.7
"	3.8	.00(.04)	.10(.06)	.00(.07)	1.0
"	5.3	.01(.04)	.11(.06)	-.03(.07)	1.2
"	8.0	.01(.03)	.10(.06)	-.01(.08)	1.1
"	10.1	.03(.04)	.06(.06)	.01(.07)	1.2
"	21.4	.06(.01)	.01(.01)	.04(.01)	1.7

Chapter 4

MODELING OF THE MULTIPOLE EVOLUTION

4.1 Introduction

An important result of this convoy electron measurement is the ability to quantitatively assess the validity of using theoretical predictions for electron excitation and ionization in ion-atom collisions for this ion-solid collision system. In this chapter, the evolution with target thickness of extracted multipole moments is modeled using atomic cross sections associated with ELC and ECC, as well as with projectile capture, ionization and excitation. Given the validity of the model to be used, these data demonstrate a unique method of testing theoretical predictions for these atomic cross sections.

As was demonstrated qualitatively in the previous chapter, the convoy electron angular distributions change dramatically over a relatively small span of target thicknesses x. This rapid evolution can be tracked quantitatively via the extracted multipole moments $\beta_k(x)$ and is attributed to changes in the relative contribution from different precursor states. In this context a precursor state refers to the state the electron occupies immediately prior to the collision which produces the convoy

electron. The basis for the following analysis is straightforward: since the data contain a superposition of multipole contributions from different precursor states, it should be possible to model the multipole evolution given that we know the multipole moment, β_k^i, and the thickness-dependent convoy yield, $Y_i^c(x)$, associated with each precursor state i. Thus, for the measured multipole moment $\beta_k(x)$, we write

$$\beta_k(x) = \frac{\sum_i \beta_k^i Y_i^c(x)}{\sum_i Y_i^c(x)}, \tag{4.1}$$

where the summation is made over the ground- and all contributing excited-states.

For the Ar^{17+} and Ar^{15+} ions, events are dominated by ELC of the "valence" electron and ECC can be neglected. For these ions the ground-state corresponds to the projectile state(s) $1s$ (and $2s$), and represents the only state(s) from which a convoy electron may be produced under SCC. The remaining states of the summation correspond to higher shells ($n > 1, 2$) which may produce convoy electrons only after a minimum of two collisions. For Ar^{18+} , ECC cannot be neglected since it is the only SCC process available to produce a convoy electron for the bare ion. In this case, the ground-state is defined as the state corresponding to a bound target electron from which the ECC electron is captured; the higher states correspond to the projectile levels $n \geq 1$ from which the two-step processes of electron capture to a bound state followed by ELC (ECLC) can occur.

4.1.1 Thickness-dependent Yields

In order to discuss the evolution of convoy electron yields from different precursor states i, it is necessary to determine the fractional population of these states as a function of thickness. The probability P^i that a projectile is in a particular charge state with electron(s) in a particular state(s) is usually described by a set of coupled linear differential equations:[67]

$$\frac{dP^i}{dx} = \sum_{j \neq i} (\sigma_j^i P^j - \sigma_i^j P^i) \tag{4.2}$$

where σ_i^j is the cross section for a transition from state i to state j, and x is the target thickness expressed in atoms per unit area. By defining a total transition cross section,

$$\sigma_i^T \equiv \sum_{j \neq i} \sigma_i^j,$$

Eq. 4.2 may be rewritten

$$\frac{dP^i}{dx} = -\sigma_i^T P^i + \sum_{j \neq i} \sigma_j^i P^j. \tag{4.3}$$

The left and right terms on the right hand side are called the sink and source terms (respectively) of the rate equation. Eq. 4.3 has the nonstationary solution[68]

$$P^i(x) = \int_0^x e^{-\sigma_i^T (x-x')} \sum_{j \neq i} \sigma_j^i P^j(x') dx'. \tag{4.4}$$

However, Eq. 4.4 is not useful without knowedge of the other state functions $P^j(x)$. In many cases only the initial conditions and transition cross sections for all the $P^i(x)$'s are known. A solution to the system of N differential equations requires finding the roots (or eigenvalues) of an N-1 order (characteristic) equation which generally cannot be done analytically for N>4. Therefore, a numerical solution of Eq. 4.3 is usually necessary to determine the evolution of P_i.

In the following two sections, two separate examples of solutions to rate equations of the form in Eq. 4.3 will be presented. In both cases, the $P^i(x)$'s will represent the probability that the projectile is in a particular state i, so that

$$\sum_i P^i(x) \leq 1. \tag{4.5}$$

In the first section, the evolution of exiting charge state fractions is modeled numerically using theoretical predictions of electron capture, loss and excitation cross sections for the σ_i^j's of Eq. 4.3. In the second section, analytic solutions are found for the state-dependent convoy electron yields (per incident ion), $Y_i^c(x)$, using approximations to Eq. 4.2.

Charge State Fractions

As described in chapter 2, measurements were made of the exiting projectile charge state fractions for 37 a.u. Ar^{15+} incident on targets of different thicknesses. The evolution of charge state fractions is governed by the linear differential equations of Eq. 4.2, where the *number* of projectile electrons and not their particular states is important. Since there are no other experimental data for this system, these measurements are important in assessing the accuracy of theoretical ionization cross sections.

In the experiment considered here, the energy was sufficiently high that the equilibrium charge state fraction of Ar^{18+} (bare) was very close to 1. Recall that the equilibrium charge state fraction is defined as the average charge state of a projectile after transit through a target of equilibrium thickness; that is, the thickness necessary to completely erase the memory of the incident charge state. Thus, for a given incident charge state ion, the incident and higher (more fully stripped) charge states should dominate the fractions in Eq. 4.3. For example with the Ar^{15+} incident beam used here, the dominant charge states should be Ar^{15+}, Ar^{16+}, Ar^{17+}, and Ar^{18+}. The ground electronic state of each of these ions will be considered first (4 P^i's) and additional excited states will be added later (8 P^i's).

Listed in Table 4.1 are theoretical cross sections for excitation and ionization of v_p=37 a.u. hydrogenic argon scaled for an atomic carbon (Z_T=6) target. The full first-Born calculations of Gillespie[69,70] for excitation and ionization from the $1s$ and $2s$ state were used to determine the σ_j^i's for this system. Gillespie has written the total cross section in terms of an overall scaling factor, $8\pi/{v_p}^2$, times an elastic (target is unchanged) plus inelastic (target is excited or ionized) collision strength. The collision strengths are tabulated explicitly only for He, N, and Ar targets, so the interpolation to atomic C was made by scaling the N elastic and inelastic collision strengths as Z_T and Z_T^2 respectively.[69] Since addition over the final state angular momenta is already made within the calculation of the collision

Table 4.1: Table of theoretical excitation, ionization and capture cross sections for 37 a.u. Ar^{17+} and Ar^{18+} + C to states of principal quantum number n. ($n = \infty$ represents an unbound electron). (1) Gillespie; first-Born; (2) PWBA; (3) CDW.[72]

n	σ_{1s}^{n} (1)	σ_{2s}^{n} (1)	σ_{n}^{∞} (2)	σ_{∞}^{n} (3)
	$(10^{-5}\mathring{A}^2)$	$(10^{-5}\mathring{A}^2)$	$(10^{-3}\mathring{A}^2)$	$(10^{-7}\mathring{A}^2)$
1	—	2.94	0.572	45.3
2	42.5	—	2.17	19.7
3	8.52	166.	6.37	7.80
4	3.17	41.2	14.3	3.72
5	1.53	17.0	21.8	2.04
⋮	⋮	⋮	⋮	⋮
∞	63.4	170.	—	—

strengths, it is only possible to extract a cross section for a transition to a particular n-level. The de-excitation cross section σ_{2s}^{1s} is also from Gillespie's results, and is assumed to be collisional in nature. Gillespie's ionization cross sections, σ_{1s}^{∞} and σ_{2s}^{∞}, agree reasonably well (within 20%) with a plane wave Born approximation (PWBA) calculation[71] for this system. For the excited-states $n > 2$, the ionization cross sections have been averaged over the low angular momentum expected after a single excitation collision (specifically $\sigma_{n}^{\infty} \equiv (\sigma_{ns}^{\infty} + \sigma_{np}^{\infty} + \sigma_{nd}^{\infty})/3$).[71]

The results of a continuum distorted wave approximated (CDW) calculation of electron capture cross sections carried out for this system by Rozet[72] are also listed in Table 4.1. As is evident from the table, these values are much smaller than the associated excitation/ionization cross sections.

It is clear that the above cross sections do not completely describe this problem, since they concern bare and one-electron ions only. Nevertheless, these values represent the best available predictions for this collision system. Furthermore,

the comparison of these cross sections with charge state fractions measured in the present experiment should give at least a rough idea of their accuracy, which will be useful since these cross sections are also needed to determine $Y_i^c(x)$. There are three 'rules of thumb' used in the application of the above cross sections to this system.

1. Each bound projectile-electron is assumed to behave independently for ionization. For example, for the ionization of Ar^{15+} to produce Ar^{16+} , the transition cross section is set equal to $2\sigma_{1s}^{\infty} + \sigma_{2s}^{\infty}$.

2. The transition cross sections associated with electron capture are set equal to Rozet's Ar^{18+} capture cross sections to the appropriate shell.[72] In this case, where only the ground states of the ions are considered, the cross section for the transition from Ar^{16+} to Ar^{15+} is set equal to σ_{∞}^{2}. Partially filled shells are also considered. For example, the cross section for capture by Ar^{17+} to produce Ar^{16+} is set equal to $\sigma_{\infty}^{1}/2$.

3. No transitions are considered which require two or more electrons to change state. For example, the cross section for a transition from Ar^{15+} to Ar^{17+} is set to 0.

Once the transition cross sections for the four states are obtained, the set of differential equations are integrated numerically using a fourth-order Runge-Kutta method.[73] The initial conditions were set so that $P^{15} = 1$ and all other $P^{i} = 0$. The resulting charge state fractions are plotted (vs. target thickness) as the dashed lines in in Figure 4.1, along with the experimental data.

While the agreement between the calculated and experimental charge state fractions is reasonable, some improvement can be made by adding a few excited-states. Since theoretical cross sections for both excitation and ionization from the $2s$ state are available, it is natural to include any excited-states containing only the $1s$ and/or $2s$ state(s). This procedure adds one excited state of Ar^{15+} ($1s2s^2$), two excited

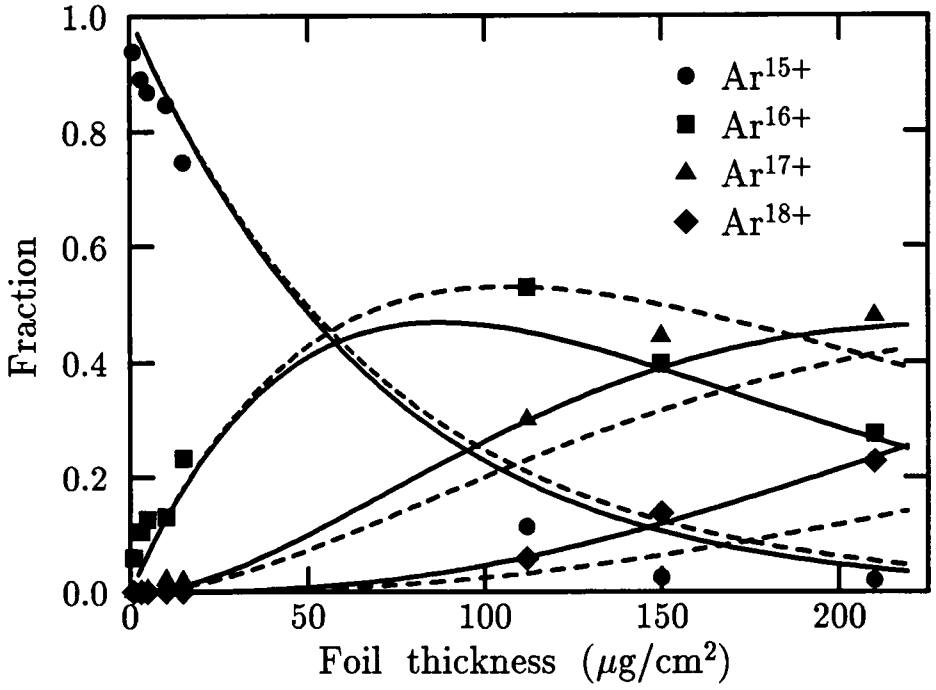

Figure 4.1: Charge state fractions of $v_p = 37$ a.u. Ar^{15+} incident on carbon foils. The dashed line represents a theoretical prediction considering only the ground states of each ion. The solid line includes low-lying excited states as well.

states of Ar^{16+} $(1s2s, 2s^2)$ and one excited state of Ar^{17+} $(2s)$ to the ground-states of each of the four charge state ions. The total charge state fraction is the sum of the ground- and excited-states of each particular charge state. The resulting charge state fractions are plotted as the solid line in Figure 4.1 using the previous rules for extraction of the implied 56 transition cross sections.

There is a marked improvement in the agreement with the addition of the excited-state terms. In the first calculation, the only ionization channel available to the bound electrons was through direct (single-step) ionization. The addition of the excited-states allows the more rapid increase in higher charge state fractions present in the experimental data by opening additional channels.

Convoy Yields

The equations governing the number of convoy electrons produced after a particular thickness x are also of the form of Eq. 4.2, where the one of the probabilities, $P^c(x)$, represents the probability that an ion is accompanied by a convoy electron within the viewing region of the experiment. From this point forward, this probability will be denoted $Y^c(x)$, since it represents the yield of convoy electrons per incident ion emitted within the measured viewing cone after a thickness x. In this section, it will be necessary to distinguish between different electronic states of the same charge state projectile, since the intrinsic multipole moments are strongly sensitive to the convoy electron's precursor state. This analysis will consider only bound states of different principal quantum number n since present theoretical cross sections are only available for excitation to states of different n.[70] The probability of an electron being in a projectile bound state n will be denoted $P^n(x)$; the probability that the electron is unbound will be denoted $P^\infty(x)$. Thus, for example, $Y^c(x)$ is a fraction of $P^\infty(x)$.

The fact that the equilibrium charge state for this system is very close to 18 (bare Ar) indicates that the cross section for electron capture is much lower than

the corresponding cross section for electron loss. This is also clear from the table in the previous section, where capture cross sections for Ar^{18+} were several orders of magnitude less than the corresponding loss cross sections of Ar^{17+} . The same argument applies for excitation and de-excitation. For example, σ_{1s}^{2s} in Table 4.1 is 2 orders of magnitude higher than σ_{2s}^{1s}. In general, for this collision system, the size of any source terms of Eq. 4.3 proportional to electron capture or de-excitation will be much smaller than the corresponding sink term. Therefore these source terms are ignored in this analysis. Under this assumption, a bound projectile electron can only make transitions to more highly-excited bound-states or to the continuum. In this case, the set of linear differential equations of the form in Eq. 2, governing the probability evolution (with thickness) of an electron occupying a particular state, may be represented by a triagonal matrix. Neglecting for the moment the "unbound" probability $P^{\infty}(x)$, these equations can be written,

$$\frac{d}{dx}\begin{pmatrix} P^1 \\ P^2 \\ P^3 \\ \vdots \\ Y^c \end{pmatrix} \approx \begin{pmatrix} -\sigma_1^T & 0 & 0 & \cdots & 0 \\ \sigma_1^2 & -\sigma_2^T & 0 & \cdots & 0 \\ \sigma_1^3 & \sigma_2^3 & -\sigma_3^T & \cdots & 0 \\ \vdots & \vdots & \vdots & \ddots & \vdots \\ \sigma_1^c & \sigma_2^c & \sigma_3^c & \cdots & -\sigma_c^T \end{pmatrix} \begin{pmatrix} P^1 \\ P^2 \\ P^3 \\ \vdots \\ Y^c \end{pmatrix}. \tag{4.6}$$

The total transition cross sections $\sigma_i^T, i = n, c$ are the eigenvalues of the matrix so that the solution to the rate equation for any particular state will involve a linear combination of $\exp(-\sigma_i^T x)$. In this equation, σ_i^T includes *all* transitions which deplete state i including any transitions to states not described above. This includes (primarily) ionization-transitions to state ∞. The total convoy transition cross section σ_c^T, which describes scattering of the convoy electron out of the viewing cone of the spectrometer, is set equal to the equivalent free-electron (inelastic) scattering cross section which, for this energy, is $\sim 4 \times 10^{-2} \mathring{A}^2$.[55]

While the solution of this system of equations provides the total yield of convoy electrons, it does not distinguish between convoys produced from different precursor states. Since convoys produced from different states have different angular distri-

butions and therefore different multipole moments, it is necessary here to consider the solution of $Y^c(x)$ when c is populated via specific channels, or a sequence of transitions. Consider N transitions from bound state $s1$ through a progression of more highly excited bound states $s2, s3, \cdots, s(N-1)$ to a final state sN $(=c)$. This type of process could occur through a progressive excitation of the projectile via multiple scattering in the bulk prior to the collision which produces the convoy electron. Furthermore, for a particular state si in this chain, let the part of $P^{si}(x)$ populated through this channel be denoted by $P^{si}_{s1,s2,\cdots,s(i-1)}(x)$. The set of equations governing these transitions can be written

$$\begin{aligned}
\frac{dP^{s1}}{dx} &= -\sigma^T_{s1} P^{s1} \\
\frac{dP^{s2}_{s1}}{dx} &= \sigma^{s2}_{s1} P^{s1} - \sigma^T_{s2} P^{s2}_{s1} \\
\frac{dP^{s3}_{s1,s2}}{dx} &= \sigma^{s3}_{s2} P^{s2}_{s1} - \sigma^T_{s3} P^{s3}_{s1,s2} \\
&\vdots \quad \vdots \\
\frac{dP^{sN}_{s1,s2,\cdots,s(N-1)}}{dx} &= \sigma^{sN}_{s(N-1)} P^{s(N-1)}_{s1,s2,\cdots,s(N-2)} - \sigma^T_{sN} P^{sN}_{s1,s2,\cdots,s(N-1)}
\end{aligned} \tag{4.7}$$

If the system is initially in state $s1$, or $P^{s1}(0) = 1$, the solutions to Eq. 4.7 may be found using Eq. 4.4:

$$\begin{aligned}
P^{s1} &= e^{-\sigma^T_{s1} x} \\
P^{s2}_{s1} &= \sigma^{s2}_{s1} \left(\frac{e^{-\sigma^T_{s1} x}}{\sigma^T_{s2} - \sigma^T_{s1}} + \frac{e^{-\sigma^T_{s2} x}}{\sigma^T_{s1} - \sigma^T_{s2}} \right) \\
P^{s3}_{s1,s2} &= \sigma^{s2}_{s1} \sigma^{s3}_{s2} \left(\frac{e^{-\sigma^T_{s1} x}}{(\sigma^T_{s2} - \sigma^T_{s1})(\sigma^T_{s3} - \sigma^T_{s1})} + \frac{e^{-\sigma^T_{s2} x}}{(\sigma^T_{s1} - \sigma^T_{s2})(\sigma^T_{s3} - \sigma^T_{s2})} \right. \\
&\quad \left. + \frac{e^{-\sigma^T_{s3} x}}{(\sigma^T_{s1} - \sigma^T_{s3})(\sigma^T_{s2} - \sigma^T_{s3})} \right) \\
&\vdots \quad \vdots \\
P^{sN}_{s1,s2,\cdots,s(N-1)} &= \left(\prod_{i=1}^{N-1} \sigma_i^{i+1} \right) \left(\sum_{j=1}^{N} \frac{e^{-\sigma^T_j x}}{\prod_{k \neq j} (\sigma^T_k - \sigma^T_j)} \right).
\end{aligned} \tag{4.8}$$

For the very thin targets used in this experiment, only a few collisions are likely to occur with any significance; the convoy emission from highly excited n states is

expected to be intense only if the electron populates these states after one or two collisions. For incident Ar^{15+} and Ar^{17+} , only one- and two-step processes involving direct ELC or excitation prior to ELC were found to contribute substantially to the overall yield in these thin targets. The one-step convoy yield (per incident ion) of Ar^{17+} is produced by ELC of the $n = 1$ electron. This yield is denoted in the model as $Y_1^c(x)$, and is described by $P_1^c(x)$ in Eq. 4.8. Similarly, the production of convoy electrons from higher bound states of Ar^{17+} , $Y_n^c(x)$, is modeled by the two-step convoy yield of Ar^{17+} , $P_{1,n}^c(x)$. Again, the three-step contributions to $Y_n^c(x)$, described by the three-step probability $P_{1,1<j<n,n}^c(x)$, are assumed to be negligible for these target thicknesses.

For the Li-like Ar^{15+} , the one- and two-step yields from the valence $2s$ electron, $Y_2^c(x)$ and $Y_n^c(x)$, are described by $P_2^c(x)$ and $P_{2,n}^c(x)$ respectively. The total yield from Ar^{15+} is obtained by adding twice the contribution from Ar^{17+} to simulate the presence of two core $1s$ electrons.

The situation is somewhat different for incident Ar^{18+} . In this case, one-, two- and three-step processes were found to contribute non-negligibly to the total yield. These processes correspond to ECC, capture to a bound state prior to ELC, and capture to a bound state prior to excitation prior to ELC. In order to see any convoy electrons, some sort of unlikely capture event must occur, either to the continuum (ECC) or to a bound state followed by ELC or excitation and ELC (ECLC). The initial state represents the bare Ar projectile and will be denoted here by $P^{\infty}(x)$. This state is initially very close to equilibrium and obviously is not described by Eq. 4.8 for the initial state $P^{s1}(x)$. However, for the thin foils considered here, there should be little if any change in $P^{\infty}(x)$ so that it may be approximated as being constant. For convenience, it will be written here as the solution for $P^{s1}(x)$ in the limit of $\sigma_{\infty}^T \rightarrow 0$. The ECC yield then becomes

$$P_{\infty}^c(x) = \frac{\sigma_{\infty}^c}{\sigma_c^T}(1 - e^{-\sigma_c^T x}), \tag{4.9}$$

and the two- and three-step ECLC yields become

$$P^c_{\infty,n}(x) = \sigma^n_\infty \sigma^c_n \left(\frac{1}{\sigma^T_n \sigma^T_c} + \frac{e^{-\sigma^T_n x}}{\sigma^T_n(\sigma^T_n - \sigma^T_c)} + \frac{e^{-\sigma^T_c x}}{\sigma^T_c(\sigma^T_c - \sigma^T_n)}\right) \tag{4.10}$$

$$P^c_{\infty,n,n'}(x) = \sigma^n_\infty \sigma^{n'}_n \sigma^c_{n'} \left(\frac{1}{\sigma^T_n \sigma^T_{n'} \sigma^T_c} + \frac{e^{-\sigma^T_n x}}{\sigma^T_n(\sigma^T_n - \sigma^T_{n'})(\sigma^T_c - \sigma^T_n)} + \frac{e^{-\sigma^T_{n'} x}}{\sigma^T_{n'}(\sigma^T_{n'} - \sigma^T_n)(\sigma^T_c - \sigma^T_{n'})} + \frac{e^{-\sigma^T_c x}}{\sigma^T_c(\sigma^T_c - \sigma^T_n)(\sigma^T_{n'} - \sigma^T_c)}\right) \tag{4.11}$$

At this point, it is necessary to determine the transition cross sections for the yield equations. The capture cross sections, σ^n_∞, are already listed in Table 4.1. Some interpolation is necessary to obtain the total transition cross sections σ^T_i. Gillespie's[69,70] results for ionization and excitation from the $1s$ and $2s$ states are used for σ^T_1 ($1.23 \times 10^{-3} \mathring{A}^2$) and σ^T_2 ($4.32 \times 10^{-3} \mathring{A}^2$), but no theoretical cross sections are available for either excitation (to all higher levels) or for ionization from $n > 2$. As n increases, σ^T_n should also increase and approach the value of $\sigma^T_c(3.09 \times 10^{-2} \mathring{A}^2)$. Furthermore, σ^T_n must be greater than the total ionization cross section σ^∞_n. Since σ^∞_n rapidly approaches σ^T_c (e.g. σ^∞_5 is already $> 70\%$ of σ^T_c!), these restrictions strongly limit the range of possible values for σ^T_n. Little difference was found in the convoy electron yields or multipole evolution as a result of varying the values of σ^T_n within these restrictions.

The only remaining unknowns in the above equations are the cross sections for production of a convoy electron, $\sigma^c_i (i = 1, 2, \cdots, \infty)$. For the ECC cross section σ^c_∞, the cross sections for bound-state capture to states of asymptotic n are used. This technique follows that of Knudsen et al.[74], and begins by integrating only the first order velocity contribution to the projectile-frame DDCS in Eq. A.1:

$$\frac{d\sigma}{dE_e} = \int \frac{d^2\sigma}{dE_e d\Omega_e} d\Omega_e = 4\pi\sigma_0. \tag{4.12}$$

This singly-differential continuum capture cross section should be continuous across the ionization threshold, so that it is possible to equate it with the bound state capture cross section

$$\frac{d\sigma}{dE_e} = \frac{d\sigma}{dn}\frac{dn}{dE_e} = (\sigma^n_\infty)(Z_p^{-2} n^3). \tag{4.13}$$

Using the "reduced capture cross section", $\sigma_c = n^3\sigma_\infty^n$ (which approaches a constant for large n), σ_0 can be written

$$\sigma_0 = \frac{\sigma_c}{4\pi Z_p^2}. \tag{4.14}$$

σ_0 is found to be 2.24×10^{-8} a.u./steradian using the CDW-calculated cross section for capture to $n = 5$ found in Table 4.1. Little difference is found using Chan and Eichler's eikonal correction to the first Born approximation[75] for calculating σ_∞^n, from which σ_0 is calculated to be 2.20×10^{-8} a.u./sr..

For the ELC cross section, Szabo[71] has explicitly calculated the cross section amplitude σ_0 for ELC from states of nl up to $n = 9$ for this collision system. Again, for excited-states $n > 2$, we have averaged over low angular momenta to determine σ_n^c. A plot of these cross sections versus the principal quantum number are displayed as solid circles in Figure 4.2, along with the ionization and capture cross sections of Table 4.1.

Finally, once σ_0 is calculated, σ_i^c is obtained by integrating the lab-frame DDCS over the range of energies and angles used for the yield measurements. In this case, the range of lab-frame energies ($\sim \pm$ 14 a.u.) and angles ($\sim \pm$ 0.56°) selected for integration of the experimental spectra correspond to approximately equal ranges of $v_{||}$ and $v_\perp$ in the projectile-frame ($\approx$ 0.73 a.u.). This symmetric range was chosen so as to minimize the effect of the anisotropic terms $\beta_k, k \neq 0$, on the total cross section (see Eq. 4.12). (In fact, the effect of including β_1 in the integration–set at any arbitrary value -1$\leq \beta_1 \leq$1–changed the total cross section by less than 0.1%.) The total cross section σ_i^c is then equal to the cross section amplitude σ_0 times a proportionality factor independent of the process (i.e. the angular distribution):

$$\sigma_i^c \approx \sigma_0(2\pi\gamma \int_{\Delta E_e} \int_0^{\theta_e} \frac{v_e}{v_e} dE_e \sin\theta_e d\theta_e) = \alpha\sigma_0. \tag{4.15}$$

In this case, α = 1.06 a.u.-steradian.

The total convoy electron yields (per incident projectile) are found by adding the one- and two-step expressions for Ar^{17+} and Ar^{15+} , and adding the one-, two-

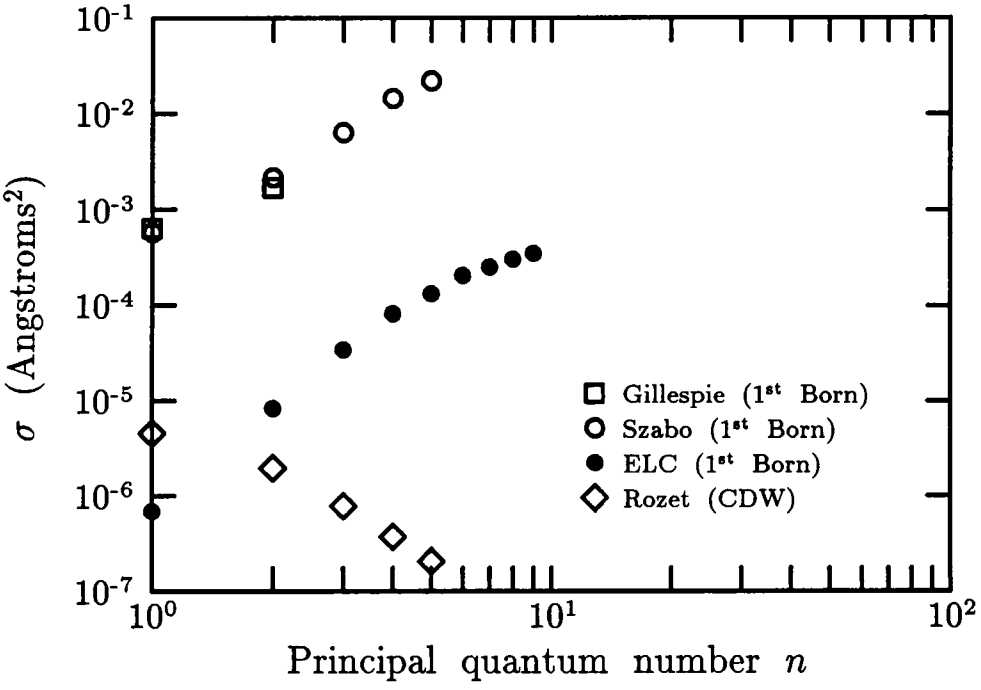

Figure 4.2: Cross sections for ELC, total ionization and capture vs. principal quantum number n. The open diamonds represent the cross sections for capture into states n summed over angular momentum l.[72] The solid circles represent ELC cross sections[71] averaged over angular momentum as described in the text. The open circles and open squares represent the total ionization cross section as a function of n as listed in Table 4.1.

and three-step functions for Ar^{18+} . These resulting yield expressions are compared with the experimental data in Figure 4.3. The yield expressions are displayed as solid lines in the graph. The experimental yields have been integrated over the range discussed above and normalized to the number of incident ions. A channel plate efficiency of 35% has been assumed for these $\sim$ 20 keV electrons[76]. The agreement between the experiment and theory is quite good, considering that no free parameters were used. In fact, the largest disagreement between the model and the data occurs in the case of Ar^{15+} incident, where the large convoy event rates made it necessary to use less incident beam current. As pointed out in Chapter 2, this made it quite difficult to obtain accurate normalization. The large scatter in the data is indicative of this problem.

4.1.2 Intrinsic Multipole Moments

An implicit assumption of this model is that the intrinsic multipole moments β_k^i are not thickness-dependent. In other words, electrons emitted at thickness x from state i have the same angular distribution exiting the target as those emitted from the same state at a different thickness x'. This argument assumes that any scattering of the convoy electrons in the bulk of the solid *after their creation* does not strongly alter their measured angular distribution. The justification of this assumption is seen by considering the perturbative effects of the projectile ion on the scattering distributions of the convoys. More specifically, the presence of the large Coulomb field of the projectile results in "Coulomb defocusing"[77]: The resulting distribution of the convoy electron after an inelastic collision in the solid is much broader than that for a free electron. If the convoy electron has momentum $\vec{p}$ prior to an inelastic collision with momentum transfer $\vec{\Delta p}$, the projectile-frame energy loss may be written:

$$\Delta E = \frac{(\vec{p} + \vec{\Delta p})^2}{2} - \frac{p^2}{2}$$

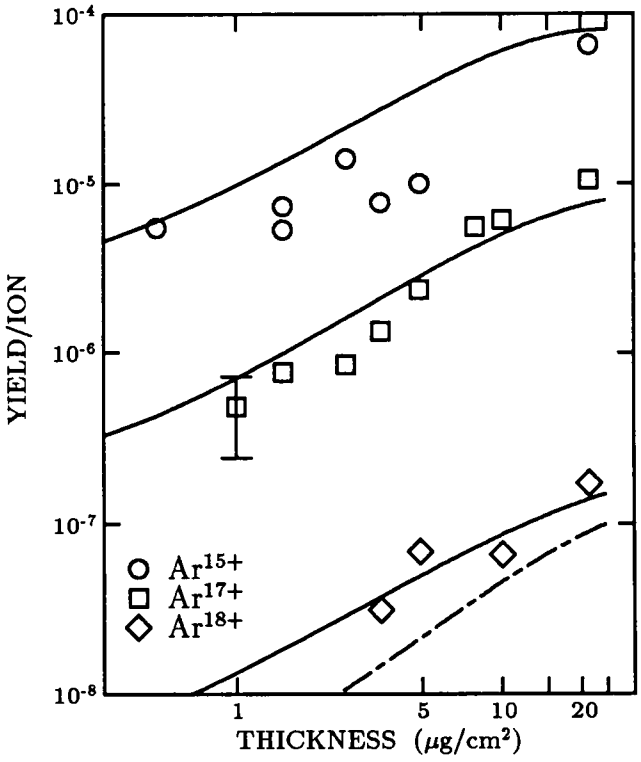

Figure 4.3: Experimental convoy yields per incident ion.

$$= \vec{p} \cdot \vec{\Delta p} + \frac{(\Delta p)^2}{2}. \tag{4.16}$$

The first term on the right hand side of Eq. 4.16 can be quite large—especially if the convoy electron is near the projectile nucleus and has a large initial momentum. At the time of the collision the convoy electron may be moving in any particular direction (i.e. in any hyperbolic continuum orbit) about the projectile so that the orientation of $\vec{p}$ is somewhat random. Thus, in addition to increasing the possible energy transfer, Eq. 4.16 allows for lab-frame energy gains as well. Since the angular momentum of the convoy electron is usually small ($l < 5$), the corresponding momentum distribution is quite large which therefore results in a large range of final energies compared to the final distribution of similarly scattered free electrons.

An example of the strong effect of Coulomb defocussing is seen in a comparison of free electron energy distributions, calculated using the technique in Section 2.2.1, and convoy electron energy distributions calculated using the Monte Carlo method. The latter method assumes a convoy electron exactly at threshold; i.e. a lab-frame velocity $v_e = v_p$. Results of this comparison are shown in Figure 4.4a-b. In Figure 4.4a, the Monte Carlo program assumed that the projectile charge $Z_p = 0$, thus simulating the free electron distribution for comparison with the transport equation solution of chapter 2. As demonstrated in the figure, the agreement is very good. In Figure 4.4b, the Monte Carlo program "turned on" the projectile charge Z_p=1 and assumed the angular momentum of the convoy electron was l = 3. Even with this low Z_p, the effect on the distribution is dramatic. Although the distribution is still peaked at small energy losses, it is so broad that most of the convoys are ejected out of a typical convoy viewing region. Thus, while it is important to consider convoy electron transport phenomena for modeling the *yield*, its effect on the *angular distributions* in the small forward cone is expected to be negligible.

Neglecting convoy electron transport effects, β_k^i should approach the multipole moment expected in an equivalent atomic collision. Extending Burgdörfer's first-

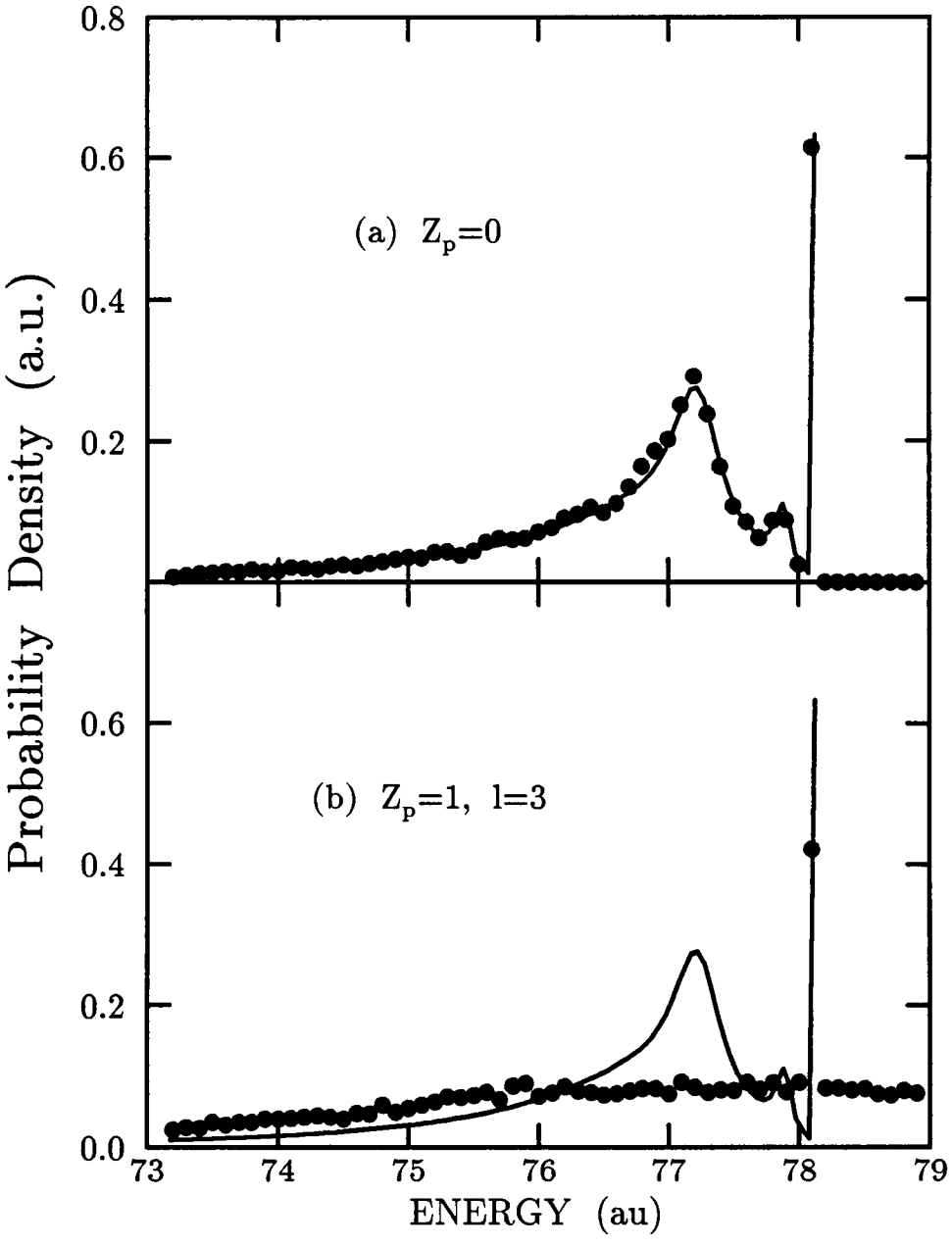

Figure 4.4: Comparison of free- and convoy-electron inelastic scattering distributions. Distributions were generated for v_p=11 a.u. mono-energetic electrons incident on a carbon target of thickness 42.5 a.u.. The solid line represents an iterative solution to the transport equation for free electrons ($Z_p = 0$) described in Section 2.2.1; the solid circles represent the results of a Monte Carlo simulation including the perturbative effects of a projectile of charge (a) $Z_p = 0$, (b) $Z_p = 1$.

Table 4.2: Table of theoretical β_k^i's for different initial states of hydrogenic Argon.[71] Odd-order coefficients are always zero in the first-Born approximation.

Projectile	(nl state)	β_2	β_4	β_6
Ar^{17+}	(1s)	0.095		
Ar^{17+}	(2s)	-0.652	0.180	
Ar^{17+}	(5s)	-1.10	0.53	-0.200

Born approximation theory for ELC anisotropy coefficients to arbitrary projectile and target charge Z_p, Z_t, Szabo[71] has calculated a few β_k^i's for this collision system. Table 4.2 lists the results of his calculation.

While the measurement made here cannot verify all of these values, the thin target results for incident Ar^{17+} and Ar^{15+} should approach (with decreasing target thickness) the parameters associated with the states $1s$ and $2s$. For the Ar^{17+} incident ion, the experimental β_2 value for the thinnest target is closer to zero than 0.095. However, it is important to remember that the first-Born approximation condition of $v_{orb} \ll v_p$ is not well met for the Argon K-shell. Indeed, the presence of the odd-order coefficients β_1, β_3, and β_5 in the data are also not predicted by the first-Born approximation.

The first-Born condition is better fulfilled for the case of Ar^{15+} incident. The experimental values of β_2 (-0.76) and β_4 (0.27) for the thinnest target (found in Table 3.1) are both a little larger than the $2s$ values predicted by Szabo. The discrepancies may be caused by the contribution of excited states $n > 2$. For example, recalling the first-Born approximation section rules introduced in Section 3.1.2, the existence of a fairly large β_6 in this dataset indicates perhaps some contribution from $n = 3$.

A model of excited-state contributions should include emission from states np, since excitation from the $1s$ and $2s$ states will also occur to dipole-transition-allowed p-states. Fortunately, while there appear to be differences in β_k^i between different

magnetic sublevels, the intrinsic multipole moments for ELC from np_1 and ns have been found to be very similar.[78] Therefore, the β_k^i values for ELC from ns were used in the modeling as the expected β_k^i values for ELC from (after excitation to) n, independent of l. A linear interpolation was made to estimate the n-levels not calculated (i.e. n=3,4).

However, it is evident from the discussion of convoy electron yields that there are significant contributions from states $n > 5$. Unfortunately, the calculation of statistical multipoles for these highly-excited states (with $\sim n$ radial nodes) is much more difficult than the corresponding calculation for the inner shells.[78] Furthermore, the (mean) orbital radius of the $n = 5$ state of Ar^{17+} equals the mean atomic lattice spacing of the amorphous C target. Thus, emission from states of larger n are more subject to the dynamical screening of the target and are probably not well described by atomic collision calculations. In this model, these asymptotic β_k^i values are simply set to the values used for emission from $n = 5$.

For ELC from states $n > 1$, where the first-Born approximation criterion is well satisfied, the dipole moments β_1^i ($i > 1$) have been set to 0. The negative values of β_1 found for Ar^{17+} incident on thin foils (see Table 3.2) imply a negative dipole moment β_1^1 associated with ELC from the $1s$ state. Also, the negative values of β_1 found for Ar^{18+} incident on thin foils imply a negative dipole moment β_1^0 associated with ECC. These two parameters which represent the SCC-dipole moments for incident Ar^{17+} and Ar^{18+} are determined by a linear extrapolation of the thin foil results to zero target thickness ($x = 0$). For Ar^{17+} , extrapolation of results of the three thinnest foils ($x = 1.4$, 1.8 and 2.2 $\mu g/cm^2$) gives $\beta_1^1 = -0.30 \pm 0.06$. For Ar^{18+} , extrapolation of the two thinnest foils ($x = 3.5$ and 5.3 $\mu g/cm^2$) gives $\beta_1^0 = -0.45 \pm 0.12$. This latter result agrees quite well the impulse approximation calculation of Jakubaßa-Amundsen[79] which predicts an ECC asymmetry coefficient of $\beta_1 = -0.44$ for Ar^{18+} + He collisions at the same velocity ($v_p = 37$ a.u.).

Finally, the higher-ordered moments β_k^0, $k > 1$, associated with ECC are expected

to be small.[64] Thus, for this model these parameters have been set to 0.

4.2 Results of the Model and Discussion

Shown in the following three figures are the results of the model for the moments β_2, β_4 and β_1. Also pictured as a function of thickness are the experimental multipole moments for incident Ar^{15+} , Ar^{17+} and Ar^{18+} . In these figures, the dashed line represents the results using the theoretical values for the intrinsic multipole moments β_k^i described in the previous section. Where shown, the solid lines represent the results after changing the β_k^i values to better match the data for thin targets.

The quadrupole moment β_2 demonstrates the largest change in magnitude versus thickness and therefore the most sensitivity to variations in the model parameters. It is clear from Figure 4.5 that the predicted values of β_2 from Szabo fail to describe the (primarily) SCC values for Ar^{17+} and Ar^{15+} . For Ar^{17+} , the data appear to approach zero instead of 0.095, suggesting a change in the value of β_2^1. Furthermore, a constant offset in the remaining values of β_2^i is implied by the good agreement between the shapes of the data and theoretical curves. Significant improvement is made by shifting the values for $\beta_2^i (i > 1)$ by ~ -0.2 to match the SCC value for Ar^{15+} incident, as can be seen in the solid curves. For Ar^{18+} , the shape of the theoretical curve and data are also quite similar, although the data is larger in magnitude. The solid line in this case represents the result when β_2^0 is changed to -0.35. While this curve does a good job reproducing the data, this value of β_2^0 is much larger than that expected for ECC.[80] Another possibility for this case is that the ECC cross section is smaller than predicted in Eq. 4.15. For example, if the ECC cross section σ_0^c is reduced by a factor 3.5, the first two data points are reasonably well reproduced by the model without changing the initial value β_2^0. This may be seen in the dot-dashed line in Fig. 4.5. However, besides the fact that there is no reason to expect such a reduction in σ_0^c, this modified model clearly fails

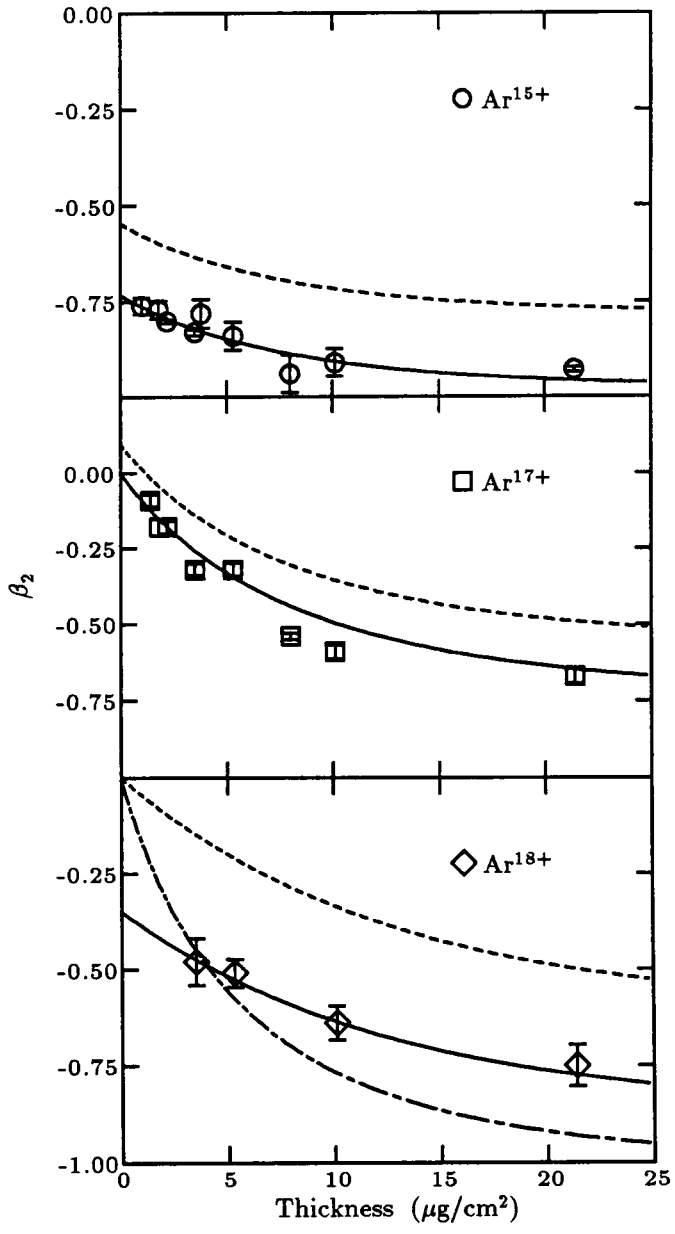

Figure 4.5: Comparison of the experimental and modeled quadrupole moment β_2. Data points and error bars are taken from the experimental results listed in Table 3.1. The solid, dashed, and broken lines represent results of the modeling as described in the text.

to match the data for the thicker targets.

In the modeling of β_4 in Figure 4.6, as in the previous case, a shift in the theoretical values of the intrinsic moments $\beta_4^i (i > 1)$ produces a large improvement in the agreement between the data and the model. Once again, the dashed lines represent the results based solely on the theoretically determined intrinsic multipole moments of the previous section—the solid lines represent the model after these values have been shifted to improve the thin target agreement. For incident Ar^{15+} , the agreement with the data is much better when the magnitude of the moments $\beta_4^i (i > 1)$ is increased by ~ 0.1, although there still remain discrepancies for the thicker targets. For both incident Ar^{17+} and Ar^{18+} , the thin target values of β_4 approach 0, as predicted. The difference in the dashed and solid lines for these two charge states are the results of the shifted values of β_4^i for ELC from excited-states introduced to obtain a better fit with the β_4 results for Ar^{15+} incident. Finally, the resulting model evolution for incident Ar^{18+} is displayed (again, as dot-dashed lines) for the case of reducing the ECC cross section by a factor 3.5, as was attempted for the β_2 model above. Again, this reduction produces a clearly inferior result.

The poorest agreement between the model results and the data is seen in Figure 4.7 of the dipole moment β_1. Dipole moments vanish for emission from excited states within the first Born criterion ($n > 1$) so that any observed evolution should equilibrate at 0. Instead, these data seem to approach positive values of β_1 at thicker targets. Physically, this corresponds to a larger number of convoy electrons emitted ahead of the projectile or, equivalently, on the high energy side of the cusp. This effect has been observed in the singly-differential energy spectra of convoy electrons and has been interpreted as resulting from the slowing-down of electrons from the binary encounter peak which occurs near $v_e = 2v_p$.[15] Unlike inelastically scattered convoy electrons, these higher energy electrons may suffer less from the Coulomb defocusing effects caused by Eq. 4.16. Since population of the cusp region by (initially) high energy electrons is not taken into account in the present model,

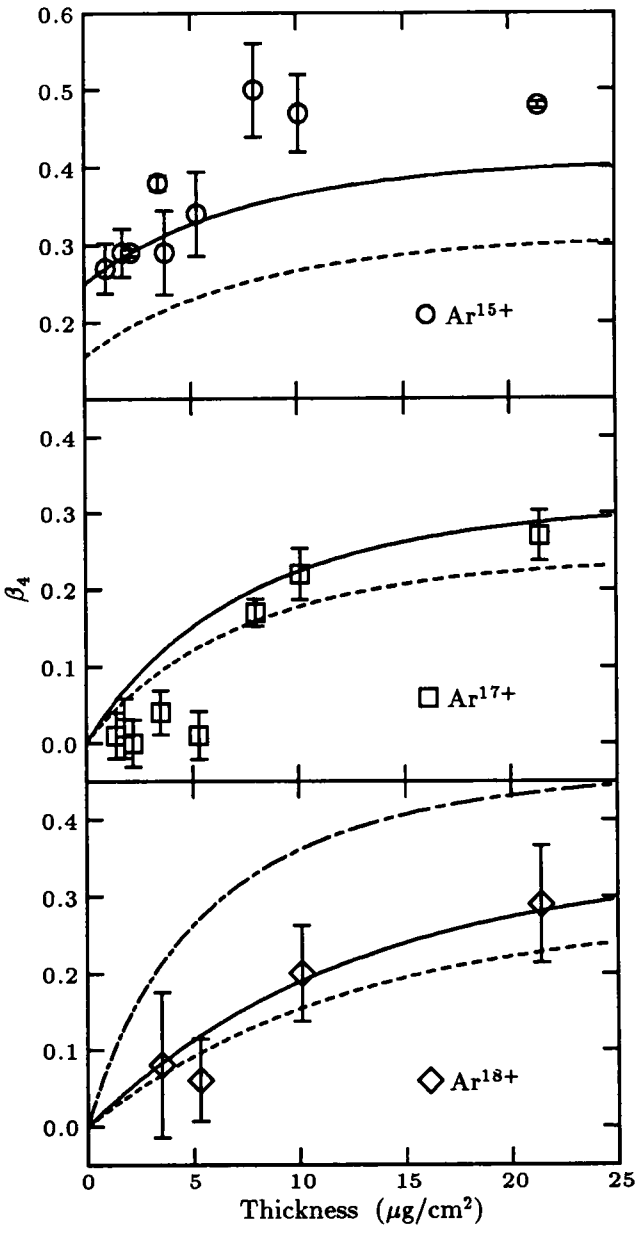

Figure 4.6: Comparison of the experimental and modelled hexadecapole moment β_4. Data points and error bars are taken from the experimental results of Table 3.1. The lines represent modeling results described in the text.

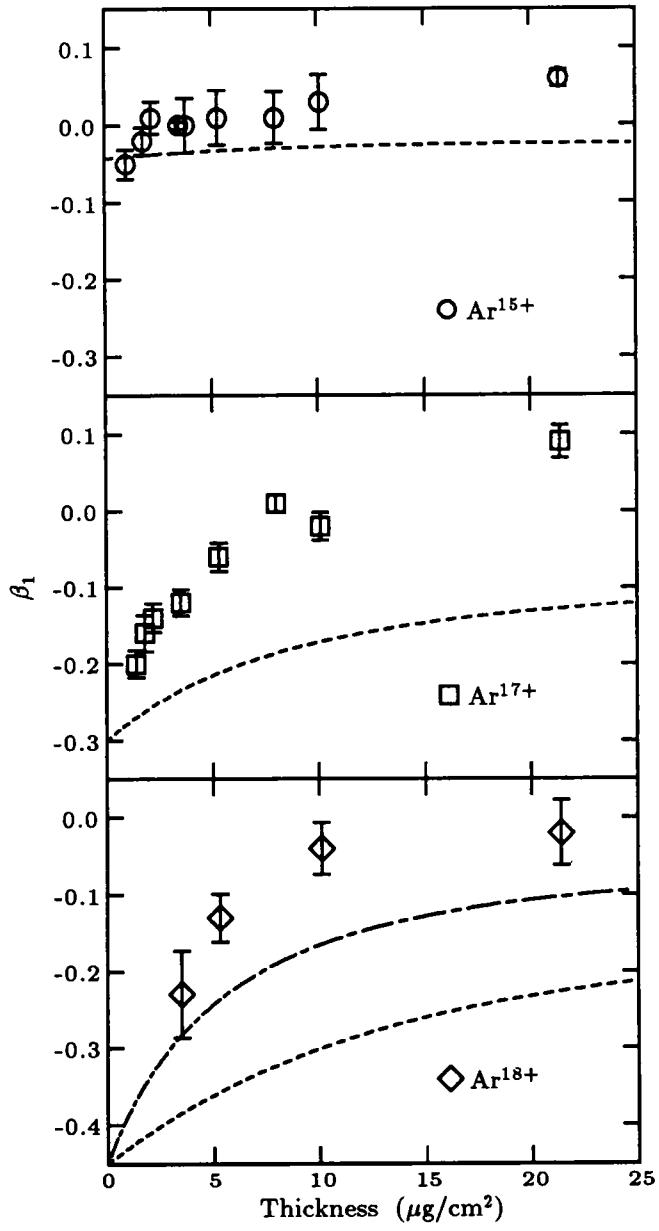

Figure 4.7: Model of the dipole moment β_1.

it is plausible that the agreement here will be worse.

In Fig. 4.7, the dashed lines represent the results using the interpolated values of β_1^1 (-0.30) and β_1^0 (-0.45) discussed in the previous section. It is clear that the data demonstrate a larger change in magnitude than the model for all incident charge states. Once again, the dot-dashed line displayed for incident Ar^{18+} represents the case of a reduction of the ECC cross section σ_0^c.

With the exception of this example, the agreement between the models of the charge state fractions, convoy yields and multipole moments, and the corresponding data, is quite good. In particular, the rate of change of β_k with thickness, $d\beta_k/dx$, is reproduced very well, even assuming a range of different values for the intrinsic multipole moments β_k^i. The disagreements between the magnitude of the extracted even-ordered moments and the corresponding values predicted by the model may be removed by shifting the intrinsic multipole moments β_k^i slightly in order to match the data at very thin target thickness. Furthermore, the discrepancies between the model and data for β_1 suggest contributions of continuum electron transport phenomena to the experimental data. Since the evolution is the consequence of multiple scattering processes, the model seems to do a credible job of describing multiple collision events in terms of sequential single collisions. In general, these results lend credence to an atomic description of collision processes inside the bulk of a solid and, therefore, represent a unique method of verifying atomic cross sections for excitation, ionization and capture. In this particular example, the set of cross sections listed in Table 4.1 do an excellent job reproducing a variety of different experimental data.

Unfortunately, because of the limited experimental beam time alloted for this experiment, it was not possible to include measurements of Ar^{18+} incident on foils thinner than 3.5 $\mu g/cm^2$. These data would be very useful since the present interpretation concerning the quadrupole moment associated with ECC seems to disagree with previous ion-atom results.[80] Furthermore, the count rates for this incident

charge state are much lower than for incident Ar^{15+} and Ar^{17+} , it would be beneficial to make relatively longer measurements in order to gather better statistics for these data. This would reduce the uncertainties associated with the extracted multipole moments and consequently in the corresponding zero-target thickness extrapolations.

BIBLIOGRAPHY

Bibliography

[1] N. Bohr, *Dan. Mat. Fys. Medd.* **18**, No. 8 (1948).

[2] H. H. Anderson and S. T. Picraux, eds., Nucl. Inst. and Meth. B**2** 1 (1984); K. Siegbahn, ed., Nucl. Inst. and Meth. B **194** 1 (1982).

[3] W. Brandt, in *Atomic Collisions in Solids*, edited by S. Datz, B. R. Appleton and C. Moak, (Plenum, New York, 1975).

[4] M Chevallier, A. Clouvas, N. V. de Castro Faria, B. Farizon Mazuy, M. J. Gaillard, J. C. Poizat, J. Remillieux, J. Désesquelles, Phys. Rev. A **41**, 1738 (1990).

[5] Hans D. Betz, Ralf Schramm, Willi Oswald, in *High-Energy Ion-Atom Collisions*, edited by D. Berényi and G. Hock, Lecture Notes in Physics Vol. 376 (Springer-Verlag, Berlin, 1991), p. 240.

[6] Sheldon Datz, in *High-Energy Ion-Atom Collisions* edited by D. Berényi and G. Hock, Lecture Notes in Physics Vol. 376 (Springer-Verlag, Berlin, 1991), p. 353.

[7] J. Burgdörfer, in *High-Energy Ion-Atom Collisions* edited by D. Berényi and G. Hock, Lecture Notes in Physics Vol. 376 (Springer-Verlag, Berlin, 1991), p. 199.; J. Burgdörfer and J. P. Gibbons, Phys. Rev. A **42**, 1206 (1990).

[8] S. D. Berry, S. B. Elston, I. A. Sellin, M. Breinig, R. DeSerio, C. E. Gonzalez-Lepera and L. Liljeby, J. Phys. B **19**, L149 (1986).

[9] W. Brandt and R. Ritchie, Nucl. Inst. & Meth. **132**, 42 (1976).

[10] F. J. Rogers H. C. Graboske, Jr., and D. J. Harwood, Phys. Rev. A **1**, 1577 (1970).

[11] H. D. Betz, D. Röschenthaller, and J. Rothermel, Phys. Rev. Lett., **50** 34 (1983).

[12] H. D. Betz, in *Forward Electron Ejection in Ion Collisions*, edited by K. O. Groeneveld, W. Meckbach, and I. A. Sellin, Lecture Notes in Physics Vol. 213 (Springer-Verlag, Berlin, 1984), p. 115.

[13] Y. Yamazaki, N. Solterfoht, P. D. Miller, H. F. Krause, P. L. Pepmiller, S. Datz, I. A. Sellin, J. N. Scheurer, S. Andriamonje, D. Bertault, J. F. Chemin, Phys. Rev. Lett. **61** 2913 (1988).

[14] V. N. Neelavathi, R. Ritchie, and Werner Brandt, Phys. Rev. Lett. **33** 302 (1980).

[15] Y. Yamazaki and N. Oda, Phys. Rev. Lett. **52**, 29 (1984).

[16] W. J. B. Oldham, Jr., Phys. Rev. **161**, 1 (1967).

[17] J. Macek, Phys. Rev. A **1**, 235 (1970).

[18] A. Salin, J. Phys. B **5**, 979 (1972).

[19] K. Dettmann, K. G. Harrison, and M. W. Lucas, J. Phys. B **7**, 269 (1974).

[20] F. Drepper and J. S. Briggs, J. Phys. B **9** 2063 (1976).

[21] J. S. Briggs and F. Drepper, J. Phys. B **11** 4033 (1978).

[22] M. G. Menendez, M. M. Duncan, F. L. Eisele, and B. R. Junker, Phys. Rev. A **15**, 80 (1977).

[23] C. R. Vane, I. A. Sellin, M. Suter, G. Alton, S. B. Elston, P. M. Griffin, and R. S. Thoe, Phys. Rev. Lett. **40**, 1020 (1978).

[24] M. Breinig, S. B. Elston, S. Huldt, L. Liljeby, C. R. Vane, S. D. Berry, G. A. Glass, M. Schauer, I. A. Sellin, G. D. Alton, S. Datz, S. Overbury, R. Laubert and M. Suter, Phys. Rev. A**25**, 3015 (1982).

[25] H. P. Hülskötter, M. Breinig, J. Burgdörfer, R. DeSerio, S. B. Elston, C. E. Gonzalez-Lepera, C. Kelbch, H. Schmidt-Böcking, I. A. Sellin, and Y. Yamazaki, Phys. Rev. A, **33** 2156 (1986).

[26] D. Röschenthaler, H. D. Betz, J. Rothermel and D. H. Jakubassa-Admundsen, J. Phys. B **16**, L233 (1983).

[27] Y. Yamazaki, H.-P. Hülskötter, M. Breinig, R. DeSerio, J. Burgdörfer, T. Underwood, J. Gibbons, and I. A. Sellin, Phys. Rev. A **34**, 4493 (1986).

[28] W. Meckbach, I.B. Nemirovsky, and C. Garibotti, Phys. Rev. A **24**, 1793 (1981).

[29] M. Lucas, W. Steckelmacher, J. Macek and J. E. Potter, J. Phys. B **13** (1980).

[30] J. S. Briggs and M. H. Day, J. Phys. B **13**, 4797 (1980).

[31] J. Burgdörfer et al., Phys. Rev A **28**, 3227 (1983).

[32] S. B. Elston, S. D. Berry, J. Burgdörfer, I. A. Sellin,, M. Breinig, R. DeSerio, C. E. Gonzalez-Lepera, L. Liljeby, K.-O. Groeneveld, D. Hofmann, P. Koschar, I.B.E. Nemirovsky, Phys. Rev. Lett., **55**, 2281 (1985).

[33] S. D. Berry, *Multipole Characterization of the Electron Loss to the Continuum Cross Section at Asymptotically High Velocities*, Ph. D. Dissertation, University of Tennessee, 1983 (unpublished).

[34] J. P. Rozet, A. Chetioui, P. Bouisset, D Vernhet, K. Wohrer, A. Touati, C. Stephan, J. P. Grandin, Phys. Rev. Lett. **58**, 337 (1987).

[35] J. Fermé, M. Gouttefangeas and the GANIL group, in *Ninth International Conference on Cyclotrons and their Applications*, 1981, p3.

[36] R. Anne, D. Bazin, A. C. Mueller, J. C. Jacmart, M. Langevin, Nucl. Inst. and Meth. A **257** 215 (1987).

[37] G. Glass, *Electron Capture to the Continuum from Atomic Hydrogen*, Ph. D. Dissertation, University of Tennessee, 1983 (unpublished).

[38] S. B. Elston, Nucl. Inst. and Meth. **B24/25**, 214 (1987).

[39] E. M. Purcell, Phys. Rev. **54** 818 (1938).

[40] K. D. Sevier, *Low Energy Electron Spectrometry*, (John Wiley, New York, 1972).

[41] Robert DeSerio, Rev. Sci. Inst. **60**, 381 (1989).

[42] I. A. Sellin, in *Beam-Foil Spectroscopy*, edited by S. Bashkin, Topics in Current Physics Vol. 1 (Springer-Verlag, Berlin, 1976), p. 265.

[43] Surface Science Laboratories, Inc., Model 239G Position Sensitive Detector, 4151 Middlefield Rd., Palo Alto, CA 94303.

[44] S. Lencinas, J. Burgdörfer, J. Kemmler, O. Heil, K. Kroneberger, N. Keller, H. Rothard, and K. O. Groeneveld, Phys. Rev. A **41**, 1435 (1990).

[45] J. Ashley, J. J. Cowan, R. H. Ritchie, V. E. Anderson, J. Hoelzl, Thin Solid Films **60**, 361 (1979).

[46] J. Lindhard, K. Dan. Vidensk. Selsk., Mat.-Fys. Medd., 28 (8) (1954) 1-57.

[47] M. W. Williams and E. T. Arakawa, J. Appl. Phys., **43** 3460 (1972).

[48] E. J. Williams, Proc. R. Soc. London, Ser. A, **125** (1929) 420.

[49] P. R. Bevington, *Data Reduction and Error Analysis in the Physical Sciences*, (McGraw-Hill, New York, 1969).

[50] P. H. Berning, in *Physics of Thin Films I*, edited by G. Hass, (Academic Press, New York, 1963), p. 69.

[51] John O. Stoner, Jr., Nucl. Inst. & Meth. A **236**, 662 (1985).

[52] T. Ferrell, private communication.

[53] K. Kimura, private communication.

[54] M. P. Seah and W. A. Dench, Surf. Interface Anal., **1**, 2 (1979).

[55] D. R. Penn, J. Electron Spectrosc. Relat. Phenom., **9**, 29 (1976).

[56] E. T. Arakawa, S. M. Dolfini, J. C. Ashley, and M. W. Williams, Phys. Rev. B **31**, 8097 (1985).

[57] C. Biedermann, private communication.

[58] K. Jacobi and J. Hoelzl, Surf. Sci., **26**, 54 (1971).

[59] R. G. Steinhardt, J. Hudis and M. L. Perlman, Phys. Rev. B **5**, 1016 (1972).

[60] S. B. Elston, unpublished.

[61] D. H. Jakubaßa-Admundsen, J. Phys. B **23**, 3335 (1990).

[62] J. Burgdörfer, private communication.

[63] J. Kemmler, O. Heil, C. Biedermann, P. Koschar, H. Rothard, K. Kroneberger, K. O. Groeneveld, A. Köver, G. Szabo, L. Gulyas, D. Berenyi, P. Focke and W. Meckbach, in *High-Energy Ion-Atom Collisions*, Lecture Notes in Physics Vol. 294 (Springer-Verlag, Berlin, 1987), p. 362.

[64] J. Burgdorfer, Phys. Rev. A **33**, 1578 (1986).

[65] S. D. Berry, G. A. Glass, I. A. Sellin, K.-O. Groeneveld, D. Hofmann, L. H. Andersen, M. Breinig, S. B. Elston, P. Engar, M. M. Schaur, N. Stolterfoht, H. Schmidt-Böcking, G. Nolte, and G. Schiwietz, Phys. Rev. A **31**, 1392 (1985).

[66] J. P. Gibbons, S. B. Elston, R. DeSerio, C. Biedermann, M. Breinig, O. Heil, H.-P. Hülskötter, H. Rothard, I. A. Sellin and C. R. Vane, Nucl. Inst. and Meth. B **40/41**, 53 (1989).

[67] H. D. Betz, Rev. Mod. Phys., **44** 465 (1972).

[68] H.-P. Hülskötter, J. Burgdörfer, and I. A. Sellin, Nucl. Inst. and Meth. B **24/25**, 147 (1987).

[69] G. Gillespie, Phys. Rev. A **18**, 1967 (1978).

[70] G. Gillespie, Phys. Rev. A **22**, 454 (1980).

[71] G. Szabo, private communication.

[72] J. P. Rozet, private communication.

[73] W. H. Press, B. P. Flannery, S. A. Teukolsky, and W. T. Vetterling, *Numerical Recipes: The Art of Scientific Computing*, (Cambridge University Press, 1985).

[74] H. Knudsen, L. H. Andersen, and K. E. Jensen, J. Phys. B **19**, 3341 (1986).

[75] F. T. Chan and J. Eichler, Phys. Rev. A **20**, 104 (1979).

[76] M. Galanti et al., Rev. Sci. Instrum. **42**, 1818 (1971); R.S. Gao, P. S. Gibner, J. H. Newman, K. A. Smith, and R. F. Stebbings, ibid **55**, 1756 (1984).

[77] J. Burgdörfer, in *High-Energy Ion-Atom Collisions*, Lecture Notes in Physics Vol. 294 (Springer-Verlag, Berlin, 1987), p. 344.

[78] J. Burgdörfer, private communication.

[79] D. H. Jakubaßa-Admundsen, *Forward Electron Ejection in Ion Collisions*, Lecture Notes in Physics Vol. 213 (Springer-Verlag, Berlin, 1984), p. 17.

[80] Lars H. Andersen, Kren E. Jensen and Helge Knudsen, J. Phys. B **19**, L161 (1986).

APPENDICES

Appendix A

Relativistic Transformation of the Differential Cross Section

In order to facilitate convolution with the angular and energy resolution functions, it is necessary to transform the projectile-frame DDCS to a lab-frame DDCS differential in energy and angle. The projectile-frame DDCS may be written[28]

$$\frac{d^2\sigma}{dE_e d\Omega_e} = \sigma_0 \sum_{j,k} \beta_{j,k} v_e^j P_k(\cos\vartheta_e), \tag{A.1}$$

where v_e and ϑ_e are the projectile-frame emission velocity and angle respectively. E_e and Ω_e represent the electron's projectile-frame energy and solid angle of emission. Since the transformation between projectile and lab frame is much simpler in velocity-space, it is helpful to write the DDCS as such. The full relativistic kinetic energy of an electron (in any frame) of speed $v = \beta c$ is (in atomic units),

$$E = (\gamma - 1)c^2; \qquad \gamma \equiv \frac{1}{\sqrt{1-\beta^2}}. \tag{A.2}$$

The differential dE is easily found from Eq. A.2 to be $\gamma^3 v dv$, so that the double differential becomes

$$dE d\Omega = \gamma^3 v dv d\Omega = \frac{\gamma^3}{v} d\vec{v}. \tag{A.3}$$

It is convenient here to define γ_e' and γ_e as the electron's relativistic factors in the projectile- and lab-frame respectively. The projectile-frame DDCS in velocity-space

can now be written:

$$\frac{d^2\sigma}{d\vec{v}_e} = \frac{\gamma_e'^3\sigma_0}{v_e}\sum_{j,k}\beta_{j,k}v_e^j P_k(\cos\vartheta_e). \tag{A.4}$$

The relationship between the volume elements $d\vec{\mathrm{v}}_\mathrm{e}$ (lab-frame) and $d\vec{v}_e$ (projectile-frame) is

$$d\vec{\mathrm{v}}_\mathrm{e} = ||M||d\vec{v}_e \tag{A.5}$$

where $||M||$ is the determinant of the Jacobian matrix between the two velocity vectors. For a projectile with velocity $\mathrm{v_p}$ aligned along $\hat{z}$, the Einstein velocity addition rules

$$\begin{aligned}\mathrm{v_{x,y}} &= \frac{v_{x,y}}{\gamma_p(1+\frac{\mathrm{v_p}v_z}{c^2})}\\ \mathrm{v_z} &= \frac{v_z+\mathrm{v_p}}{1+\frac{\mathrm{v_p}v_z}{c^2}}\end{aligned} \tag{A.6}$$

are used to determine the Jacobian:

$$M = \frac{1}{\gamma_\mathrm{p}(1+\frac{\mathrm{v_p}v_z'}{c^2})}\begin{pmatrix}1 & 0 & \beta_p\gamma_\mathrm{p}{}^2v_x\\ 0 & 1 & \beta_p\gamma_\mathrm{p}{}^2v_y\\ 0 & 0 & \frac{1}{\gamma_p(1+\frac{\mathrm{v_p}v_z}{c^2})}\end{pmatrix} \tag{A.7}$$

The lab-frame volume element of Eq. A.5 becomes:

$$d\vec{\mathrm{v}}_\mathrm{e} = \frac{d\vec{v}_e}{\gamma_\mathrm{p}{}^4(1+\frac{\mathrm{v_p}v_{ez}}{c^2})^4} \tag{A.8}$$

so that the lab-frame velocity-space DDCS becomes

$$\frac{d^2\sigma}{d\vec{\mathrm{v}}_\mathrm{e}} = \gamma_\mathrm{p}{}^4(1+\frac{\mathrm{v_p}v_{ez}}{c^2})\frac{\gamma_e'^3}{v_e}\sigma_0\sum_{j,k}\beta_{j,k}v_e^jP_k(\cos\vartheta_e). \tag{A.9}$$

Finally, the lab-frame DDCS, differential in $\mathrm{E_e}$ and Ω_e (the lab-frame electron energy and solid angle) may be found with the use of Eq. A.3:

$$\frac{\mathrm{d}^2\sigma}{\mathrm{dE_e d}\Omega_\mathrm{e}} = \gamma_\mathrm{p}{}^4(1+\frac{\mathrm{v_p}v_{ez}}{c^2})\frac{\gamma_e'^3\mathrm{v_e}}{\gamma_\mathrm{e}{}^3v_e}\sigma_0\sum_{j,k}\beta_{j,k}v_e^jP_k(\cos\vartheta_e). \tag{A.10}$$

In the above equation no assumptions have been made about the electron's lab- or projectile-frame velocity. However, by definition the projectile-frame velocity of

the convoy electron is quite small—usually ≤ 1 a.u.. Many of the above quantities may thus be simplified:

$$\gamma_e' \longrightarrow 1 + O(\frac{v_e^2}{c^2}) \tag{A.11}$$

$$1 + \frac{\mathrm{v_p} v_{ez}}{c^2} \longrightarrow 1 + O(\beta_p \frac{v_e}{c}). \tag{A.12}$$

Since $\beta_p < 1$, the correction in Eq. A.12 is less than 1%. It is also clear that $\gamma_\mathrm{e} \rightarrow \gamma_p$. Using the result above, the difference in γ_e and γ_p may be written:

$$\begin{aligned} \gamma_\mathrm{e} - \gamma_\mathrm{p} &= (1 - \tfrac{(\mathrm{v_p}+v_e)^2}{c^2})^{-1/2} - (1 - \tfrac{\mathrm{v_p}^2}{c^2})^{-1/2} \\ &= (1 + \tfrac{(\mathrm{v_p}+v_e)^2}{2c^2} - \cdots) - (1 + \tfrac{\mathrm{v_p}^2}{2c^2} - \cdots) \\ &\approx 0 + O(\beta_p \tfrac{v_e}{c}). \end{aligned} \tag{A.13}$$

The DDCS for near-threshold processes then becomes

$$\frac{\mathrm{d}^2\sigma}{\mathrm{dE_e d}\Omega_\mathrm{e}} \approx \gamma \sigma_0 \frac{\mathrm{v_e}}{v_e} \sum_{j,k} \beta_{j,k} v_e^j P_k(\cos\vartheta_e), \tag{A.14}$$

where $\gamma \equiv \gamma_\mathrm{p}$.

Appendix B

Relativistic Transformation of v_e, $\cos\vartheta_e$ and $d(\cos\theta_e)$

Using the approximation in Eq. A.12 to simplify the velocity addition rules in Eq. A.6, the lab-frame velocity components can be written:

$$\begin{aligned}(\mathrm{v_e})_{x,y} &= \mathrm{v_e}\sin\theta_e \approx \frac{v_e\sin\vartheta_e}{\gamma} \\ (\mathrm{v_e})_z &= \mathrm{v_e}\cos\theta_e \approx v_e\cos\vartheta_e + \mathrm{v_p}\end{aligned} \tag{B.1}$$

It is convenient at this point to introduce the dimensionless variables $z = v_e/\mathrm{v_p}$ and $\rho = \mathrm{v_e}/\mathrm{v_p}$. Solving for z in the above equations gives the expression

$$z = \sqrt{(\rho^2 - 2\rho\cos\theta_e + 1) - \beta^2\gamma^2\sin^2\theta_e}, \tag{B.2}$$

where the second term is the relativistic correction to the dimensionless projectile-frame velocity. Solving Eqs. B.1 instead for $\cos\vartheta_e$ gives the expression

$$\begin{aligned}\cos\vartheta_e &= \frac{1}{\beta^2 z}\left(-1 + \sqrt{1 - \beta^2(\frac{z^2}{\gamma^2} + 1 - \rho^2)}\right) \\ &= \frac{1}{\beta^2 z}\left(-1 + 1 - \frac{\beta^2}{2}(\frac{z^2}{\gamma^2} + 1 - \rho^2) + \frac{\beta^4}{8}(\frac{z^2}{\gamma^2} + 1 - \rho^2)^2 - \cdots\right) \\ &\approx \frac{f(\rho,\gamma)}{z} + g(\rho,\gamma)z\end{aligned} \tag{B.3}$$

where the functions $f(\rho,\gamma)$ and $g(\rho,\gamma)$ are defined as

$$\begin{aligned} f(\rho,\gamma) &= \frac{\rho^2-1}{2}\left(1+\frac{\beta^2(\rho^2-1)}{4}\right) \\ g(\rho,\gamma) &= \frac{-1}{2\gamma^2}\left(1+\frac{\beta^2(\rho^2-1)}{2}\right). \end{aligned} \tag{B.4}$$

Now that the argument of the Legendre polynomial is proportional to z and $1/z$, it is convenient to integrate over z. To write the differential $d\cos\theta_e$ in terms of dz, it is necessary to use the full velocity addition relation in Eq A.6. After some straightforward algebra, the differential may be rewritten

$$d\cos\theta_e \approx \frac{2gz}{\rho\gamma^2(1+\beta^2 f)^2}dz. \tag{B.5}$$

VITA

John P. Gibbons, Jr. was born in Huntsville, Alabama on June 27, 1963. He attended elementary and secondary schools there, graduating from Virgil I. Grissom High School in May 1981. In August of that year he entered the University of North Carolina at Chapel Hill and graduated in May 1985 with a Bachelor of Science degree with a major in Physics.

In June 1985 he entered the Graduate School of the University of Tennessee, Knoxville. He has worked on the Doctor of Philosophy degree with a major in Physics since that time, under the supervision of Professors Stuart B. Elston and Ivan A. Sellin within the University of Tennessee Atomic Physics Group, working on a variety of problems in atomic collisions in ions and solids.

The author is a member of Sigma Pi Sigma and the American Physical Society. Mr. Gibbons will be employed by The University of Minnesota Hospital, Minneapolis, Minnesota after graduation.